

Morphological diversification and functional maturation of human astrocytes in glia-enriched cortical organoid transplanted in mouse brain

Received: 21 October 2022

Accepted: 30 January 2024

Published online: 28 February 2024

 Check for updates

Meiyan Wang^{1,7}, Lei Zhang^{1,7}, Sammy Weiser Novak², Jingting Yu^③, Iryna S. Gallina¹, Lynne L. Xu^①, Christina K. Lim^{1,4}, Sarah Fernandes^{①,4}, Maxim N. Shokhirev³, April E. Williams^③, Monisha D. Saxena¹, Shashank Coorapati¹, Sarah L. Parylak¹, Cristian Quintero^⑤, Elsa Molina^⑤, Leonardo R. Andrade^②, Uri Manor^{①,2,6} & Fred H. Gage^{①✉}

Astrocytes, the most abundant glial cell type in the brain, are underrepresented in traditional cortical organoid models due to the delayed onset of cortical gliogenesis. Here we introduce a new glia-enriched cortical organoid model that exhibits accelerated astrogliogenesis. We demonstrated that induction of a gliogenic switch in a subset of progenitors enabled the rapid derivation of astroglial cells, which account for 25–31% of the cell population within 8–10 weeks of differentiation. Intracerebral transplantation of these organoids reliably generated a diverse repertoire of cortical neurons and anatomical subclasses of human astrocytes. Spatial transcriptome profiling identified layer-specific expression patterns among distinct subclasses of astrocytes within organoid transplants. Using an *in vivo* acute neuroinflammation model, we identified a subpopulation of astrocytes that rapidly activates pro-inflammatory pathways upon cytokine stimulation. Additionally, we demonstrated that CD38 signaling has a crucial role in mediating metabolic and mitochondrial stress in reactive astrocytes. This model provides a robust platform for investigating human astrocyte function.

Astrocytes comprise the most abundant glial cell type in the human brain, and their dysfunction has been implicated in numerous neurological disorders¹. However, our ability to elucidate the roles of astrocytes in brain development and in the pathogenesis of brain disorders has been limited by the scarcity of accessible human astrocytes in a brain environment. Brain organoid models have emerged as valuable tools for

investigating human brain development and disorders, as they exhibit self-organized properties that recapitulate certain aspects of the developing human brain^{2–6}. Nonetheless, current cortical brain organoid systems have limitations in efficiently generating astrocytes^{7,8}, mainly due to the extended time required for the progenitor cells to acquire glial competency⁹. In human cortical organoid systems, astrogliogenesis

¹Laboratory of Genetics, The Salk Institute for Biological Studies, La Jolla, CA, USA. ²Waitt Advanced Biophotonics Core, The Salk Institute for Biological Studies, La Jolla, CA, USA. ³Integrative Genomics and Bioinformatics Core, The Salk Institute for Biological Studies, La Jolla, CA, USA. ⁴Division of Biological Sciences, University of California, San Diego, La Jolla, CA, USA. ⁵Next Generation Sequencing Core, The Salk Institute for Biological Studies, La Jolla, CA, USA. ⁶Present address: Division of Biological Sciences, University of California, San Diego, La Jolla, CA, USA. ⁷These authors contributed equally: Meiyan Wang, Lei Zhang. ✉e-mail: gage@salk.edu

begins gradually at 3 months of differentiation and undergoes a maturation process lasting over a year⁷. Attempts to accelerate astrocyte differentiation from human-induced pluripotent stem cells (hiPSCs) have shown promise either by transiently overexpressing a critical gliogenic factor^{10,11} or by triggering a gliogenic switch with a specific set of patterning factors^{12,13}. However, it remains unclear whether these patterning factors can be successfully applied to a cortical organoid patterning paradigm to generate glia-enriched cortical organoids.

Cells or organoids cultured *in vitro* also lack blood circulation and the cortical organization of the brain. The brain is a highly vascularized organ that is connected with the systemic circulation. Astrocyte projections form glia limitans surrounding the vessels, regulating the communication between the brain and circulation and maintaining brain homeostasis^{14,15}. Transplantation of human brain organoids into rodent brains enables the successful survival, integration and formation of functional circuits of the human brain organoids *in vivo*^{16–22}.

In this study, we present a glia-enriched cortical organoid model that facilitates accelerated astrogliogenesis. By triggering a gliogenic switch in 28–33% of the cells in the organoids at 3 weeks of differentiation, we achieved efficient derivation of astroglia comprising 25–31% of the cell population by 8–10 weeks of differentiation. To investigate astrocyte function in a brain environment, we used an intracerebral transplantation method¹⁶ that yielded highly vascularized *in vivo* brain organoids. The organoid transplants displayed robust integration into the host brain and developed anatomically defined morphological subclasses of human astrocytes. Spatial genomics further revealed layer-specific molecular signatures among different subclasses of human astrocytes. Moreover, we observed the formation of perivascular astrocytic endfeet ensheathing the vessels within the transplants. Using single-nucleus RNA-sequencing (snRNA-seq), we found advanced maturation of astrocytes in our organoid transplants compared to cortical organoid transplants. Additionally, we showed that differentially expressed genes (DEGs) associated with acute reactivity exhibited significant heterogeneity across astrocyte subpopulations in an *in vivo* model of acute neuroinflammation. Notably, we demonstrated that the metabolic and mitochondrial stresses in reactive astrocytes were mediated through CD38 signaling and that treatment with a potent CD38 inhibitor effectively alleviated a wide range of stresses induced by inflammation in astrocytes.

Results

Rapid astrogliogenesis in glia-enriched cortical organoids

Astrocytes, like neurons and oligodendrocytes, originate from the radial glial cells in the subventricular zone. Because astrogliogenesis occurs late during development⁸, most brain organoid models do not develop astrocytes until a very late stage. We hypothesized that triggering an early gliogenic switch in a subset of progenitors during neuroectoderm specification would enable rapid derivation of glial cells in a human cortical brain organoid model (Fig. 1a and Extended Data Fig. 1a). To induce an early gliogenic switch, we supplemented the neuroectoderm induction media with the previously reported gliogenic agent platelet-derived growth factor (PDGF)-AA and cultured the organoids in astrocyte medium^{12,13} (Fig. 1a). Organoids cultured under the gliogenic condition demonstrated robust upregulation of gliogenic factor nuclear factor IA (NFIA) at 3 weeks of differentiation (Fig. 1b,c and Extended Data Fig. 1b), indicating early glial patterning in a subset of progenitor cells, whereas forebrain organoids cultured under published methods^{23,24} had almost no detectable NFIA expression at the same time point (Fig. 1b,c). As early as 8 weeks of differentiation, glia-enriched cortical organoids had substantially greater gliogenesis compared to the forebrain organoids, supported by the upregulation of astrocyte markers glial fibrillary acidic protein (GFAP) and HepaCAM (Fig. 1d–g and Extended Data Fig. 1c). In addition to astrocytes, robust neurogenesis was observed at 8 weeks of differentiation (Extended Data Fig. 1d). Compared to organoids cultured in a serum-free condition,

glia-enriched cortical organoids cultured in differentiation media containing fetal bovine serum (FBS) displayed the most efficient derivation of astrocytes at 3 months of differentiation (Extended Data Fig. 1e,f).

To identify cell-type diversity in glia-enriched cortical organoids, we carried out snRNA-seq on nuclei isolated from 10-week-old organoids generated from two pluripotent stem cell (PSC) lines. We first applied uniform manifold approximation and projection (UMAP) dimensionality reduction and Louvain clustering to the snRNA-seq datasets, identifying multiple neuronal and glial subpopulations (Fig. 1h, Extended Data Fig. 2a–c and Supplementary Table 1). The majority of excitatory neurons were committed to a cortical identity, characterized by the expression of cortical neuronal markers (for example, CTIP2, CUX2 and SATB2; Extended Data Figs. 1d and 2b,c). Astroglia comprised 25–31% of the total population; 5–8% of these were proliferating progenitor cells and 20–23% were astrocytes (Extended Data Fig. 2a–c). To contextualize early neurogenesis and gliogenesis in a systems-level framework, we applied a single-cell weighted gene co-expression network analysis (WGCNA)^{25,26}. By computing the average expression of 50 neighboring cells from each major cell type, we constructed co-expression networks for the astrocytes from the snRNA-seq dataset and identified two astrocyte gene modules (Fig. 1i,j, Extended Data Fig. 2d,e and Supplementary Table 2). The hub genes of astrocyte module M12 consisted of genes that function in cell–cell adhesion (*TJPI*, *ID3* and *FGFR1*), and the hub genes of module M14 consisted of many known glial markers, including transcriptional factors ZBTB20 and GLI3 and glutamate transporter SLC1A3 (Fig. 1k). Similarly, we constructed co-expression networks for the cortical excitatory neurons and identified four co-expression gene modules highly expressed in these cells (Extended Data Fig. 2f–j and Supplementary Table 3). Collectively, transcriptomic analysis of 10-week-old glia-enriched cortical organoids confirmed robust neurogenesis and astrogliogenesis.

Protoplasmic astrocytes are the most abundant astrocyte subtypes in the gray matter and exhibit highly ramified processes²⁷. Astrocyte morphogenesis depends on direct interaction with neuronal processes²⁸. We hypothesized that our organoid model supports robust astrocyte morphogenesis. To study the morphological characteristics of astrocytes during organoid differentiation, we transduced glia-enriched cortical organoids with GFAP::GFP adeno-associated virus (AAV) and carried out Sholl analysis and morphological analyses of virus-labeled astrocytes (Fig. 1l–n). Astrocytes exhibited process-bearing morphology at 3 months of differentiation and displayed robustly increased branch complexity over time, such as an increased number of primary processes, number of branches and total length of the processes (Fig. 1l–n). Immunostaining confirmed that AAV-transduced astrocytes expressed many mature astrocyte markers, and their processes were closely associated with synapses (Extended Data Fig. 3a–e). Furthermore, AAV-transduced astrocytes were capable of glutamate uptake (Extended Data Fig. 3f). Taken together, these data indicate the successful generation of functional astrocytes *in vitro*.

Formation of astrocyte morphological subclasses *in vivo*

To better mimic the endogenous microenvironment, we performed intracerebral transplantation of 8- to 10-week-old glia-enriched cortical organoids into a cavity made in the retrosplenial cortex of immunodeficient (NOD.Cg-*Prkdc*^{scid} *Il2rg*^{tm1Wjl}/SzJ or NSG) mice (Fig. 2a). Glia-enriched cortical organoids exhibited robust integration into the lesion cavity (Fig. 2b,c and Extended Data Fig. 4a–d). Immunostaining confirmed that nearly all NeuN and GFAP expression in the transplants coincided with HuNuclei expression and human GFAP (hGFAP) expression, respectively (Extended Data Fig. 4a,b), indicating that neurons and astrocytes in the transplants were derived nearly exclusively from the human organoids. Human astrocytes exhibit a notably intricate morphology in contrast to their rodent counterparts²⁹. Stereotactic viral labeling of astrocytes with GFAP::GFP AAV revealed that human astrocytes in the transplants differed from the host astrocytes in that

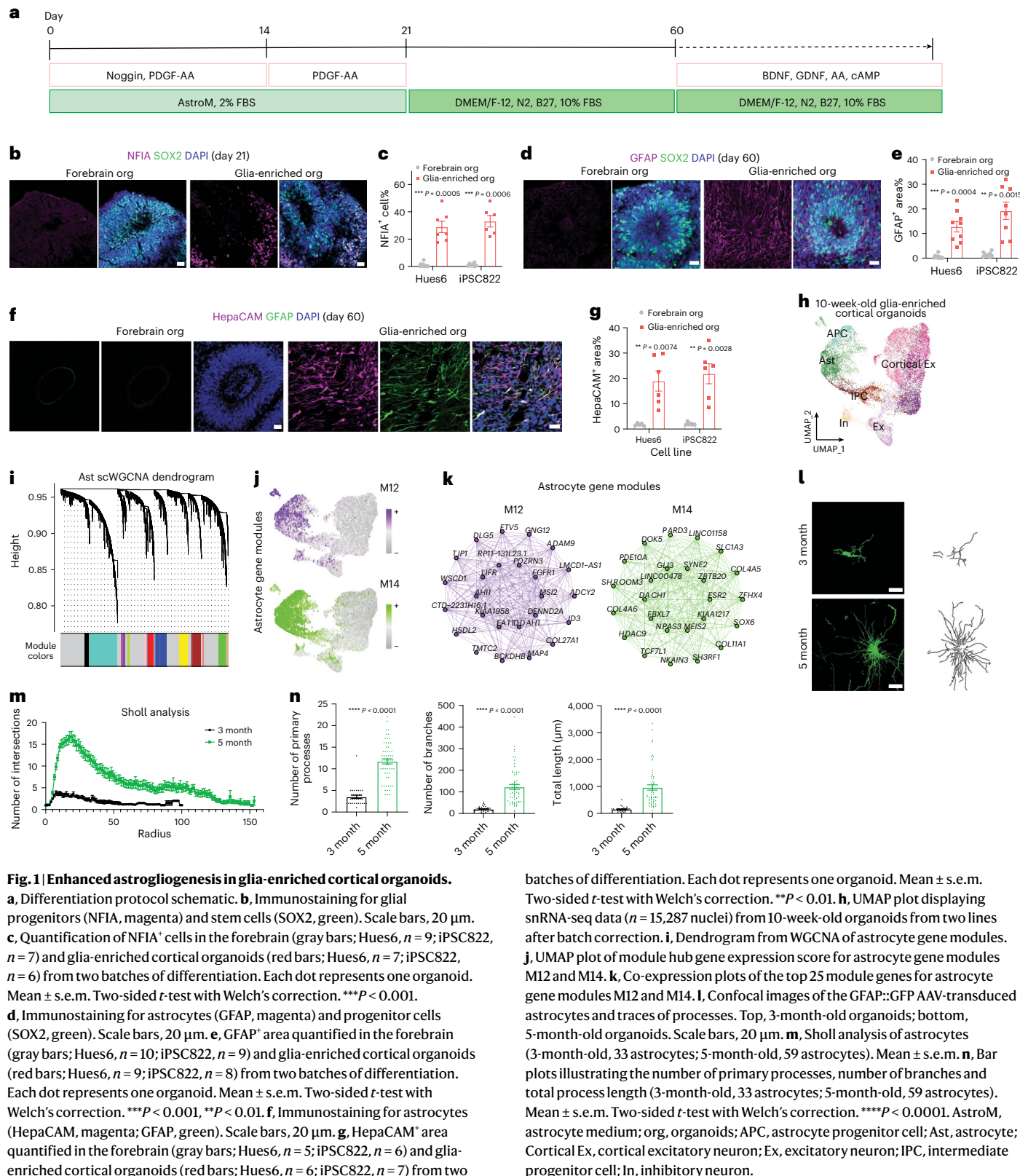


Fig. 1 | Enhanced astrogliogenesis in glia-enriched cortical organoids.

a. Differentiation protocol schematic. **b.** Immunostaining for glial progenitors (NFIA, magenta) and stem cells (SOX2, green). Scale bars, 20 μ m. **c.** Quantification of NFIA⁺ cells in the forebrain (gray bars; Hues6, $n = 9$; iPSC822, $n = 7$) and glia-enriched cortical organoids (red bars; Hues6, $n = 7$; iPSC822, $n = 6$) from two batches of differentiation. Each dot represents one organoid. Mean \pm s.e.m. Two-sided *t*-test with Welch's correction. *** $P < 0.001$. **d.** Immunostaining for astrocytes (GFAP, magenta) and progenitor cells (SOX2, green). Scale bars, 20 μ m. **e.** GFAP⁺ area quantified in the forebrain (gray bars; Hues6, $n = 10$; iPSC822, $n = 9$) and glia-enriched cortical organoids (red bars; Hues6, $n = 9$; iPSC822, $n = 8$) from two batches of differentiation. Each dot represents one organoid. Mean \pm s.e.m. Two-sided *t*-test with Welch's correction. *** $P < 0.001$, ** $P < 0.01$. **f.** Immunostaining for astrocytes (HepaCAM, magenta; GFAP, green). Scale bars, 20 μ m. **g.** HepaCAM⁺ area quantified in the forebrain (gray bars; Hues6, $n = 5$; iPSC822, $n = 6$) and glia-enriched cortical organoids (red bars; Hues6, $n = 6$; iPSC822, $n = 7$) from two batches of differentiation. **h.** UMAP plot displaying snRNA-seq data ($n = 15,287$ nuclei) from 10-week-old organoids from two lines after batch correction. **i.** Dendrogram from WGCNA of astrocyte gene modules. **j.** UMAP plot of module hub gene expression score for astrocyte gene modules M12 and M14. **k.** Co-expression plots of the top 25 module genes for astrocyte gene modules M12 and M14. **l.** Confocal images of the GFAP::GFP AAV-transduced astrocytes and traces of processes. Top, 3-month-old organoids; bottom, 5-month-old organoids. Scale bars, 20 μ m. **m.** Sholl analysis of astrocytes (3-month-old, 33 astrocytes; 5-month-old, 59 astrocytes). Mean \pm s.e.m. **n.** Bar plots illustrating the number of primary processes, number of branches and total process length (3-month-old, 33 astrocytes; 5-month-old, 59 astrocytes). Mean \pm s.e.m. Two-sided *t*-test with Welch's correction. **** $P < 0.0001$.

Astrocytes (3-month-old, 33 astrocytes; 5-month-old, 59 astrocytes). Mean \pm s.e.m. Two-sided *t*-test with Welch's correction. **** $P < 0.0001$. **a.** Differentiation protocol schematic. Each dot represents one organoid. Mean \pm s.e.m. Two-sided *t*-test with Welch's correction. ** $P < 0.01$. **h.** UMAP plot displaying snRNA-seq data ($n = 15,287$ nuclei) from 10-week-old organoids from two lines after batch correction. **i.** Dendrogram from WGCNA of astrocyte gene modules. **j.** UMAP plot of module hub gene expression score for astrocyte gene modules M12 and M14. **k.** Co-expression plots of the top 25 module genes for astrocyte gene modules M12 and M14. **l.** Confocal images of the GFAP::GFP AAV-transduced astrocytes and traces of processes. Top, 3-month-old organoids; bottom, 5-month-old organoids. Scale bars, 20 μ m. **m.** Sholl analysis of astrocytes (3-month-old, 33 astrocytes; 5-month-old, 59 astrocytes). Mean \pm s.e.m. **n.** Bar plots illustrating the number of primary processes, number of branches and total process length (3-month-old, 33 astrocytes; 5-month-old, 59 astrocytes). Mean \pm s.e.m. Two-sided *t*-test with Welch's correction. **** $P < 0.0001$. **o.** UMAP plot displaying snRNA-seq data ($n = 15,287$ nuclei) from 10-week-old organoids from two lines after batch correction. **p.** Dendrogram from WGCNA of astrocyte gene modules. **q.** UMAP plot of module hub gene expression score for astrocyte gene modules M12 and M14. **r.** Co-expression plots of the top 25 module genes for astrocyte gene modules M12 and M14. **s.** Confocal images of the GFAP::GFP AAV-transduced astrocytes and traces of processes. Top, 3-month-old organoids; bottom, 5-month-old organoids. Scale bars, 20 μ m. **t.** Sholl analysis of astrocytes (3-month-old, 33 astrocytes; 5-month-old, 59 astrocytes). Mean \pm s.e.m. **u.** Bar plots illustrating the number of primary processes, number of branches and total process length (3-month-old, 33 astrocytes; 5-month-old, 59 astrocytes). Mean \pm s.e.m. Two-sided *t*-test with Welch's correction. **** $P < 0.0001$.

the human protoplasmic astrocytes were far more elaborate and larger (Fig. 2d,e). In addition, human protoplasmic astrocytes extended long processes to the vasculature, whereas the rodent astrocytes formed rosette-like structures around the vasculature (Fig. 2f). Collectively, these results suggest that human protoplasmic astrocytes maintain their characteristic species-specific features in the transplants.

Studies revealed intrinsic differences between human astrocytes and those of lower mammals^{30,31}, including anatomically defined subclasses of human astrocytes that are absent in rodents²⁹. Besides the predominant protoplasmic astrocytes, at least three additional major morphological subclasses of GFAP⁺ astrocytes have been identified in the adult human temporal lobe, including interlaminar astrocytes,

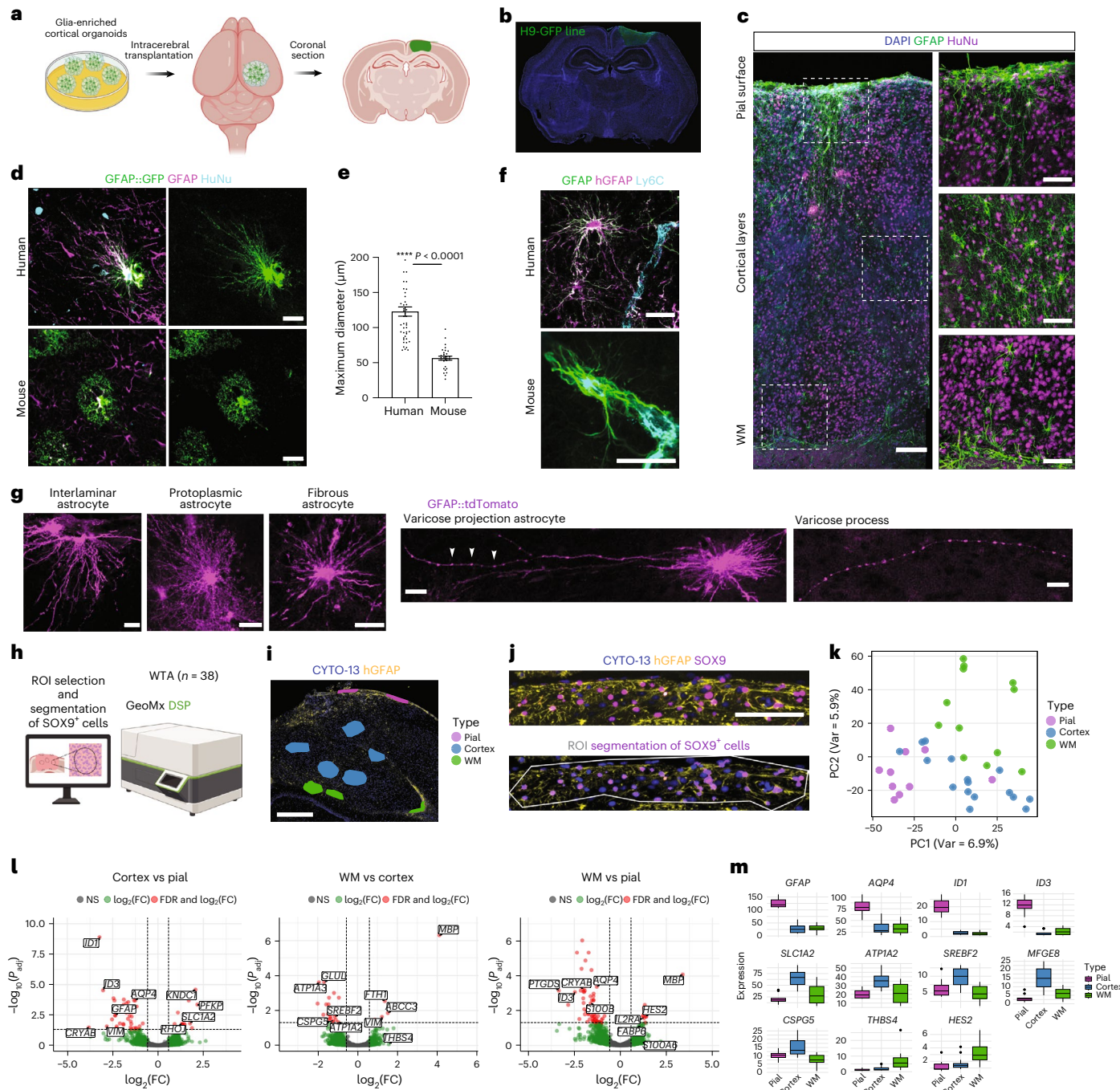


Fig. 2 | Human astrocytes form anatomically defined morphological subclasses in vivo. **a**, Illustration depicting the experimental procedure. **b**, Immunostaining for H9-GFP-derived transplant (GFP, green) and nuclei (DAPI, blue). **c**, Immunostaining of 6-month-old transplants: astrocytes (GFAP, green), human nuclear antigen (HuNu, magenta). Top inset: interlaminar astrocytes; middle inset: protoplasmic astrocytes; bottom inset: fibrous astrocytes. Scale bars, 100 μm (left) and 50 μm (right). **d**, Immunostaining of GFAP::GFP AAV-transduced astrocytes: human nuclear antigen (HuNu, cyan), astrocytes (GFAP, magenta). Top: human astrocytes; bottom: mouse astrocytes. Scale bars, 20 μm . **e**, Maximal diameter comparison of GFAP::GFP AAV-transduced human and mouse cortical astrocytes. Mouse, $n = 30$ from three mice; human, $n = 46$ from three transplants. Mean \pm s.e.m. Two-sided t -test with Welch's correction. *** $P < 0.0001$. **f**, Immunostaining for human (top; hGFAP⁺ (magenta) and GFAP⁺ (green)) and mouse (bottom; hGFAP⁺ (magenta) and GFAP⁺ (green)) astrocytes and blood vessels (Ly6C, cyan). Scale bars, 20 μm . **g**, GFAP::tdTomato

lentivirus-labeled human astrocytes in transplants (tdTomato, magenta). Arrowheads, varicosities in astrocyte processes. Scale bars, 20 μm . **h**, Overview of the GeoMx DSP workflow. **i**, Immunofluorescence staining image of one brain section with overlying selected ROIs. Scale bar, 750 μm . Thirty-eight ROIs (pial = 10, cortex = 16, WM = 12) from four sections were analyzed. **j**, Top: immunofluorescence staining for hGFAP (yellow), SOX9 (magenta) and CYTO-13 (blue). Bottom: cell segmentation of SOX9⁺/CYTO-13⁺ cells within ROI. Scale bar, 100 μm . **k**, PCA plot of GeoMx DSP gene expression data. Points: segmented SOX9⁺/CYTO-13⁺ cells per ROI, colored by location. **l**, Volcano plots of DEGs between astrocyte groups. Dashed lines, adjusted P value < 0.05 (linear mixed effect model with Benjamini–Hochberg multiple correction) and $\log_2(\text{FC}) > 1.5$. **m**, Box plots depicting the normalized expression levels of selected genes in each group (pial = 10, cortex = 16 and WM = 12). Centerline, median; box limits, upper and lower quartiles; whiskers, 1.5× interquartile range; points, outliers.

fibrous astrocytes and varicose projection astrocytes²⁹. We identified primate-specific interlaminar astrocytes at the pial surface of the transplant-forming fibers that both contributed to the glial limitans at the pial surface and penetrated deeper layers of the transplants. We also observed abundant ramified protoplasmic astrocytes in cortical layers of the transplants and fibrous astrocytes in deep layers of the transplants adjacent to white matter (WM), with relatively unbranched, straight GFAP⁺ processes (Fig. 2c and Extended Data Fig. 4e). Notably, the formation of morphological subclasses of astrocytes in the transplants was accompanied by differential expression of CD44 and S100B (Extended Data Fig. 4f,g). To further explore the morphological subclasses of GFAP⁺ astrocytes, we used GFAP::tdTomato lentiviral-transduced organoids for transplantation. Viral labeling enabled the identification of far more astrocytic processes than immunohistochemistry for GFAP (Fig. 2g). Viral labeling also revealed human- and higher-order primate-specific varicose projection astrocytes, characterized by long fibers with prominent varicosities (Fig. 2g). Together, these results show that intracerebral transplantation creates a permissive environment for the specification of anatomically defined human astrocyte subclasses.

To decipher the molecular signatures of astrocytes across transplant layers, we next spatially profiled the expression of human protein-coding genes on formalin-fixed paraffin-embedded (FFPE) sections using the NanoString GeoMx human whole-transcriptome atlas (WTA; > 18,000 genes) assay³² (Fig. 2h). We first selected the regions of interest (ROIs) across different transplant layers (that is, pial, cortex and WM) and then performed segmentation of astrocytes within each ROI according to SOX9⁺ staining (Fig. 2i,j and Extended Data Fig. 5a). Using principal component analysis (PCA), we observed separations in the gene expression profiles between layer-specific astrocytes (Fig. 2k). Comparative transcriptomic analysis revealed that expression levels of many established astrocyte markers varied according to their specific locations (Fig. 2l,m, Extended Data Fig. 5b and Supplementary Tables 4–6). Pial interlaminar astrocytes demonstrated elevated expression levels of astrocyte markers, such as GFAP, aquaporin 4 (AQP4) and transcriptional repressors ID1 and ID3 (Fig. 2l,m). Meanwhile, fibrous astrocytes within the WM displayed increased expression of thrombospondin 4 (THBS4) and transcription factor HES2, and cortical gray matter (predominantly protoplasmic) astrocytes demonstrated elevated expression of solute carrier family 1 member 2 (SLC1A2), ATPase Na⁺/K⁺ transporting subunit α-2 (ATP1A2), sterol regulatory element-binding transcription factor 2 (SREBF2) and neuroglycan C (CSPG5; Fig. 2l,m). We then carried out gene set enrichment analysis (GSEA) and identified that cortical (predominantly protoplasmic) astrocytes exhibited enrichment in genes associated with steroid metabolism, cholesterol biosynthesis, neurotransmitter release cycle and nervous system development, highlighting their close interaction with neurons (Extended Data Fig. 5c). To further explore the interactions between astrocytes and neurons, we confirmed the expression of glutamate transporter EAAT2 (gene name SLC1A2) and synaptogenic protein HEVIN (gene name SPARCL1) in human protoplasmic astrocytes by immunostaining (Extended Data Fig. 6a,b). Electron microscopy (EM) revealed the presence of multi-synaptic boutons (Extended Data Fig. 6c), indicating neuronal maturation in the transplants. To investigate the physical proximity of synapses and astrocytes in the transplants, we used serial-sectioning EM and reconstructed a dendrite with spines (Extended Data Fig. 6d). We observed astrocytic processes surrounding the synapse (Extended Data Fig. 6e), indicating a close association of human astrocytes with synapses in vivo. Collectively, these findings demonstrate the functional diversification of astrocyte subclasses at the molecular level.

Human astrocytes form perivascular astrocytic endfeet

In the brain, astrocytes are uniquely positioned to interact with both neurons and the vasculature. We observed an extensive host

vascular network and microglia infiltrating into the transplants (Extended Data Fig. 6f–i). Unlike the in vitro astrocytes, protoplasmic astrocytes in the transplants established spatial territory (Fig. 3a,b). Astrocytic processes interact with blood vessels through cap-like cytoplasmic processes called astrocytic endfeet. Specific channels and transporters, for example, AQP4 and Kir4.1, are targeted to astrocyte endfeet to control water and ion homeostasis at the vessel–neuron interface¹⁵. Immunostaining for the water channel protein AQP4 demonstrated polarized expression at the endfeet of the human astrocytes in the transplants, in sharp contrast to the in vitro astrocytes (Fig. 3c). This finding was further confirmed by the expression of the inward-rectifier potassium channel Kir4.1 at the perivascular astrocyte endfeet processes and of the glucose transporter Glut-1 at the astrocyte–vessel interface (Extended Data Fig. 6j,k). These results provide evidence that the in vivo environment facilitates the formation of astrocytic endfeet structure.

We next carried out EM to transplants derived from the GFP-transduced H9 hESC line to investigate the interaction between human astrocytes and host vasculature. Blood vessels were directly labeled by transcardiac perfusion with a fluorescent lipophilic carbocyanine dye that incorporates into endothelial cell membranes upon contact³³ (Extended Data Fig. 6l). The structure of the blood vessels was well maintained when examined under scanning electron microscopy (SEM), where tight junctions and marginal folds were clearly visible between endothelial cells (Fig. 3d). Glycogen granules and intermediate filament were also found in the astrocytes surrounding the vessels (Fig. 3e). We next reconstructed elements of a blood vessel and perivascular astrocytes from a 3-μm segment of a capillary found near the center of the transplant using serial section EM (Fig. 3f,g and Supplementary Video 1). Tight junctions were visible between endothelial cells in the electron micrograph (Extended Data Fig. 6m). Astrocytic processes wrapped around the vessel and apparently covered the entire surface, suggesting the formation of glia limitans surrounding the vasculature. Together, these results demonstrate the close coupling of human astrocytes to the host vasculature.

Enhanced cell maturation in engrafted organoids

To systematically investigate neuronal and glial development and maturation, we carried out snRNA-seq on 5-month-old in vitro organoids, 5-month-old transplants, 6-month-old transplants and 8-month-old transplants from two PSC lines (Fig. 4a). We first performed batch-correction integration and UMAP dimensionality reduction, identifying subpopulations of neuronal and glial cells (Fig. 4b,c, Extended Data Fig. 7a–c and Supplementary Table 7). We next leveraged a transfer learning strategy to integrate our dataset into a published atlas of postmortem prefrontal cortex samples from individuals spanning fetal, neonatal, infancy, childhood, adolescence and adult stages of development³⁴, and we estimated the cell states and their developmental stages in our organoid nuclei (Extended Data Fig. 7d–g). Most organoid nuclei from 5-month-old organoids aligned with fetal populations of the reference dataset (Fig. 4d). Notably, with transplantation and increasing organoid age, more nuclei displayed characteristics of postnatal cells (Fig. 4d), in particular upper-layer (UL) excitatory neurons, with 6.1% of ULs for the 5-month organoids aligned to postnatal stages, compared with 30.2% for the 5-month transplants and 94.5% for the 8-month transplants (Extended Data Fig. 7h).

To determine the genes involved in astrocyte development and function, we constructed co-expression networks using astrocytes from the integrated snRNA-seq data and identified an astrocyte gene module (M5) containing genes associated with glutamate transport (Fig. 4e,f, Extended Data Fig. 8a,b and Supplementary Table 8). Analysis of the harmonized module score of gene module M5 in astrocytes revealed increased expression of the module genes in the transplants compared to the in vitro organoids (Fig. 4g). We next curated the top 50 expressed genes from the upregulated gene list in mature human

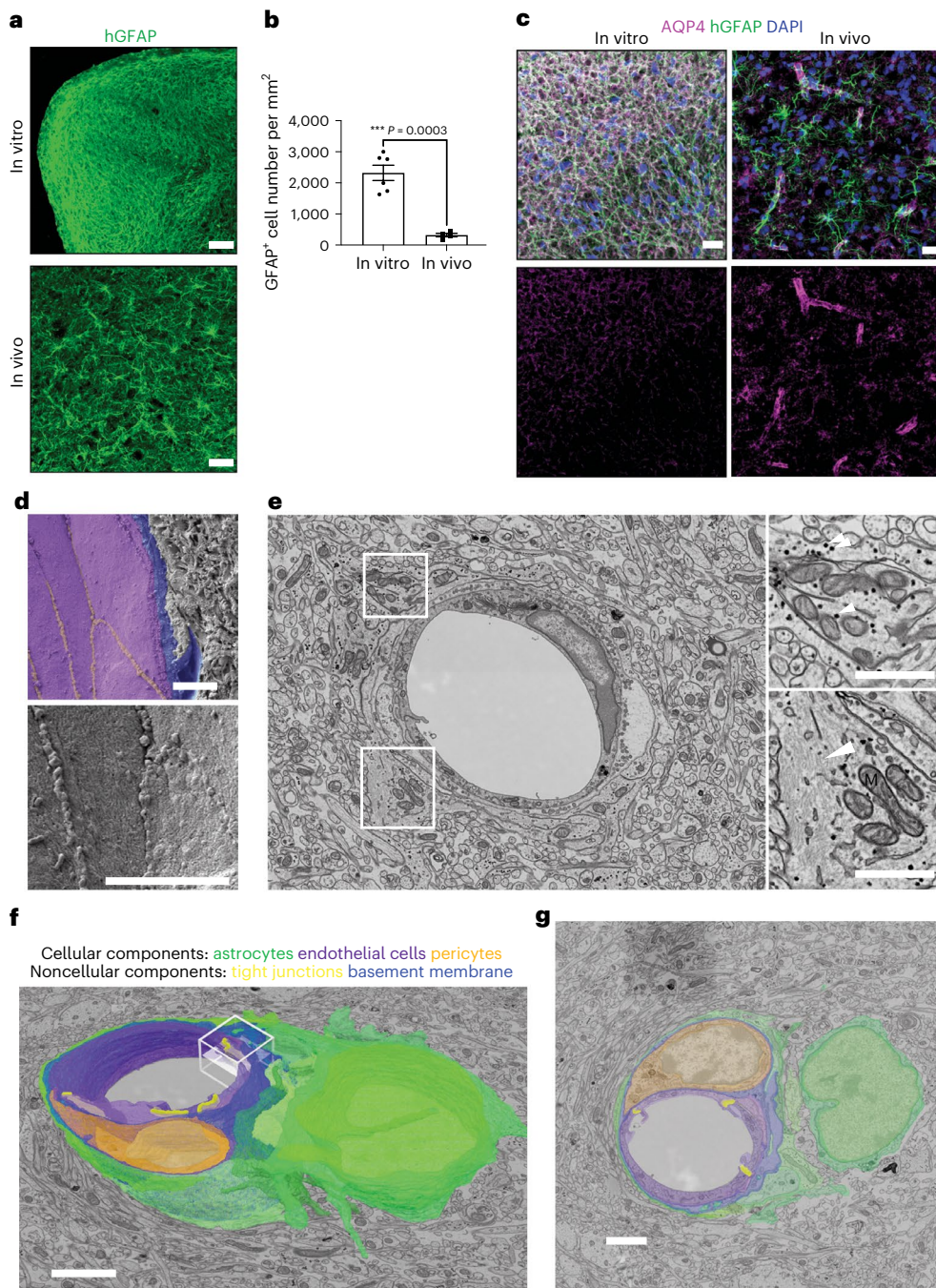


Fig. 3 | Human astrocytes form perivascular endfeet in vivo. **a**, Confocal images comparing in vitro glia-enriched cortical organoids (top, 6-month-old) and organoid transplants (bottom, 6-month-old). Immunostaining for human astrocytes (hGFAP, green). Scale bars, 100 μ m. **b**, Quantification of the number of hGFAP⁺ cells per mm² in glia-enriched cortical organoids in vitro (left) and transplants in vivo (right). $n = 6$ organoids in vitro and $n = 4$ transplants (in vivo). Two-sided t-test with Welch's correction. ***P = 0.0003. Bars, mean \pm s.e.m. **c**, Confocal images comparing glia-enriched cortical organoids in vitro (left, 6-month-old) and transplants in vivo (right, 6-month-old). Immunostaining for human astrocytes (hGFAP, green) and water channel AQP4 (magenta). Scale bars, 20 μ m. **d**, Electron micrograph of the lumen of a blood vessel in an 8-month-old

transplant captured using a scanning electron microscope. Top: endothelial cells (purple), basement membrane (blue) and intercellular leaflets (yellow). Bottom: enlarged view from the top panel. Scale bars, 4 μ m. **e**, Electron micrograph of a capillary in the transplant. Boxes show astrocyte processes. Top-right: arrowheads indicate glycogen granules. Bottom-right: an arrowhead indicates glia filaments (GFAP). Scale bars, 1 μ m. M, mitochondria. **f,g**, Electron micrograph of a capillary consists of endothelial cells (purple), tight junctions (yellow), pericytes (brown) and basement membrane (blue). The vessel was wrapped by astrocytic processes (green). Astrocyte soma (light green). Three-dimensional reconstruction of segmented data from serial section EM (**f**); pseudocolored 2D image (**g**). Scale bars, 2 μ m.

astrocytes versus fetal human astrocytes as reported in ref. 30, and we identified elevated expression of the mature human astrocyte genes in the transplants compared to the in vitro organoids (Fig. 4h,i). To further uncover glial heterogeneity and maturity, we performed pseudotime trajectory analysis using monocle 3 (ref. 35) on the integrated

snRNA-seq data in glia (Fig. 4j). Setting progenitors as the starting time point for astrocytes, pseudotime trajectory analysis revealed more cells toward the endpoint of the trajectory in the transplants, progressing from glial progenitors to astrocytes (Fig. 4j). Similarly, WGCNA and pseudotime analyses of immature and mature UL excitatory neurons

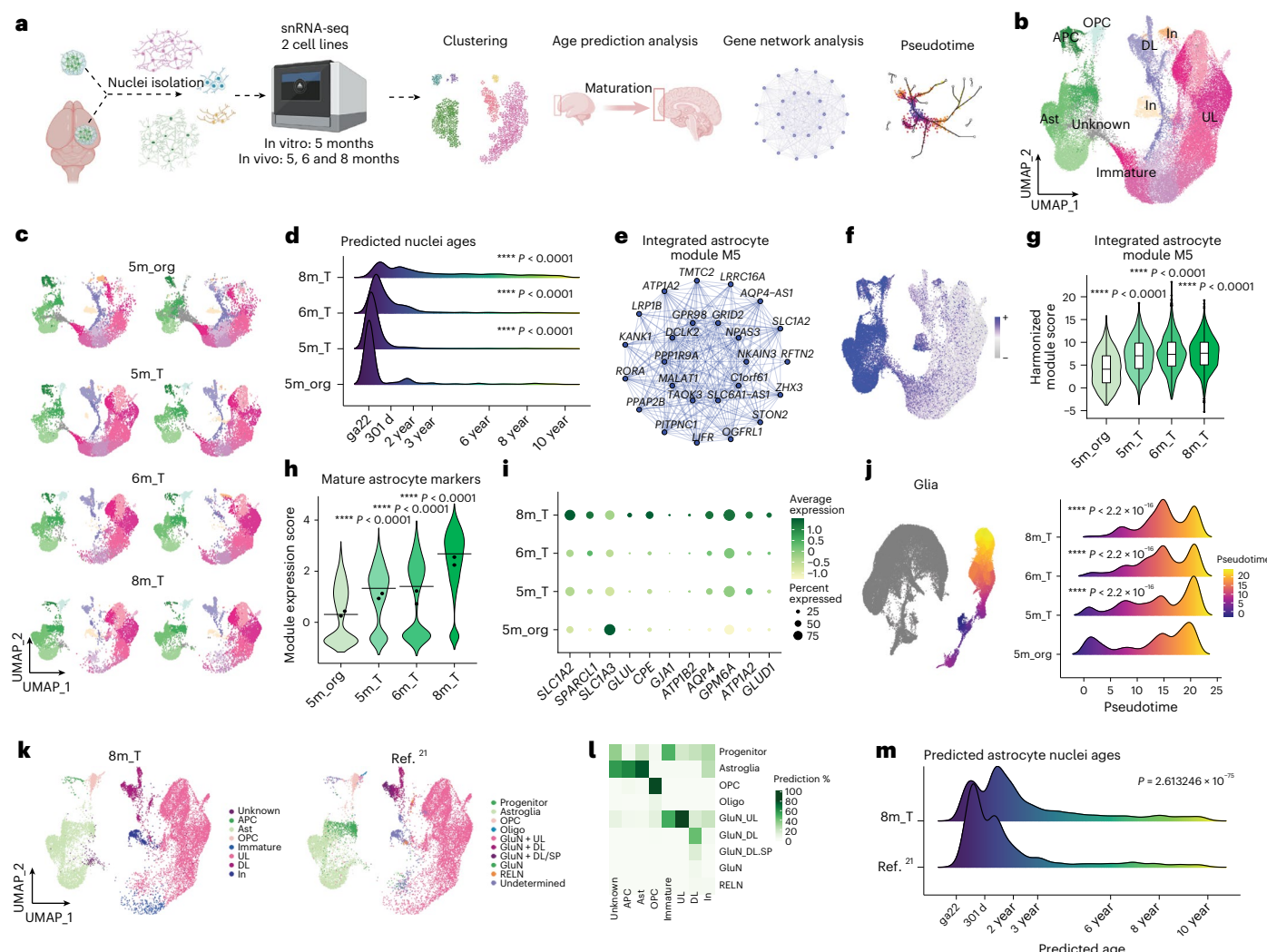


Fig. 4 | Advanced maturation of astrocytes in engrafted organoids revealed by snRNA-seq analyses. **a**, Schematic representation of snRNA-seq and related analyses. **b**, UMAP plot of snRNA-seq data ($n = 65,743$ nuclei) from 5-month-old glia-enriched cortical organoids (5m_{org}, $n = 17,490$ nuclei), 5-month-old transplants (5m_T, $n = 15,936$ nuclei), 6-month-old transplants (6m_T, $n = 15,607$ nuclei) and 8-month-old transplants (8m_T, $n = 16,710$ nuclei) from two lines after batch correction. **c**, UMAP plots of snRNA-seq data separated by individual samples. **d**, Ridge plot of predicted nuclei ages separated by time point. Wilcoxon test (two-sided, *** $P < 0.0001$; reference group, 5m_{org}). **e**, Co-expression plot of top 25 module hub genes. **f**, UMAP plot of module hub gene expression score for astrocyte module M5. **g**, Violin plot of harmonized module score of astrocyte module M5 in astrocytes across different time points. Wilcoxon test (two-sided, *** $P < 0.0001$; reference group, 5m_{org}). Centerline, median; box limits, upper and lower quartiles; whiskers, 1.5× interquartile range; points, outliers. **h**, Module expression score of mature astrocyte genes curated from ref. 30 in astrocytes

separated by each time point. Each dot represents the median value per cell line. Wilcoxon test (two-sided, *** $P < 0.0001$; reference group, 5m_{org}). **i**, Dot plot showing the expression of selected mature astrocyte genes reported in ref. 30. **j**, UMAP dimensionality reduction of astrocytes from the integrated snRNA-seq. Each cell is colored by its pseudotime trajectory assignment. Pseudotime analysis separated by time point. One-sided Kolmogorov-Smirnov test (*** $P < 2.2 \times 10^{-16}$; reference group, 5m_{org}). **k**, Projection of cortical organoid transplant snRNA-seq nuclei (ref. 21; right) onto the reference nuclei (8m_T, left). **l**, Heatmap of predicted cell type of cortical organoid transplants (ref. 21) onto the reference nuclei (8m_T). **m**, Ridge plot of predicted ages of astrocyte nuclei from 8-month-old glia-enriched cortical organoid transplants (8m_T) and cortical organoid transplants (ref. 21). Wilcoxon test (two-sided, *** $P = 2.613246 \times 10^{-75}$). APC, astrocyte progenitor cell; Ast, astrocyte; OPC, oligodendrocyte progenitor cell; In, inhibitory neuron; DL, deep-layer cortical excitatory neuron; Immature, immature excitatory neuron; UL, upper-layer cortical excitatory neuron.

revealed more advanced excitatory neuronal maturation in vivo (Extended Data Fig. 8c–g and Supplementary Table 9). Collectively, these results provide evidence that transplantation facilitates organoid maturation.

To compare the cell states of our organoid transplants with previously reported cortical organoid transplants²¹, we integrated snRNA-seq data from the cortical organoid transplants into our dataset and conducted a cell-type prediction analysis. The analysis confirmed a high degree of similarity in cell-type identity between our 8-month-old organoid transplants and the 8-month-old cortical organoid transplants²¹ (Fig. 4k,l). We then focused on examining the distribution of astrocyte nuclei ages using the age-prediction analysis.

Our differentiation paradigm supported enhanced astrocyte maturation, with 75.8% of the nuclei aligned to postnatal cells over the age of 301 d, as estimated through molecular equivalence using the brain reference dataset, compared to 56.2% of nuclei in previously reported cortical organoid transplants (Fig. 4m). Overall, these data suggest that our differentiation paradigm enhances astrocyte maturation.

Characterization of pro-inflammatory pathways in astrocytes
Reactive astrocytes are induced by central nervous system (CNS) injuries and diseases³⁶, as characterized by the upregulation of genes that can modulate CNS inflammation^{1,37} and the formation of a glial scar after CNS trauma³⁸. Despite substantial progress in our understanding of

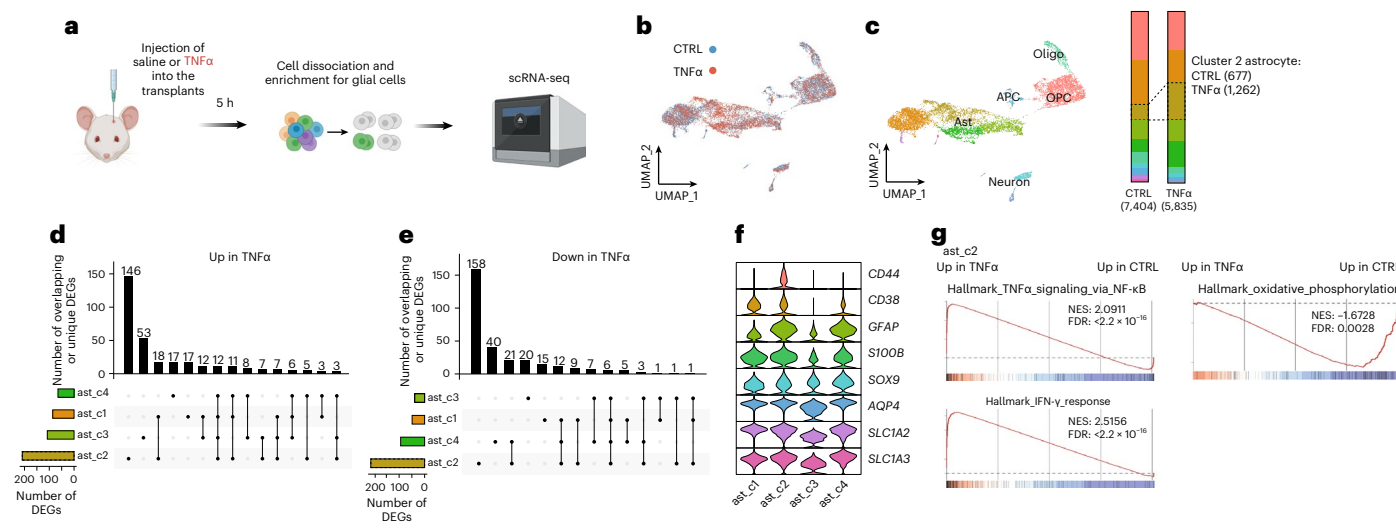


Fig. 5 | Transcriptome profiling reveals rapid activation of pro-inflammatory pathways in a subpopulation of astrocytes in vivo. **a**, Schematic representation of the experimental design. **b**, UMAP plot of scRNA-seq data from saline-treated transplants ($n = 7,404$ cells) and TNF α -treated transplants ($n = 5,835$ cells) after batch correction. **c**, UMAP plot displaying all Seurat clusters (left) and the number of cluster 2 astrocytes in each condition. **d,e**, UpSetR

plots showing the upregulated DEGs (**d**) and downregulated DEGs (**e**) that are unique to or shared between astrocyte clusters 1–4. **f**, Violin plot illustrating the expression of selected genes in astrocyte clusters 1–4. **g**, GSEA comparing TNF α -treated and saline-treated cluster 2 astrocytes. Hallmark gene sets are shown. NES, normalized enrichment score; IFN- γ , interferon-gamma.

this pronounced transformation process, our knowledge of astrocyte reactivity has been predominantly based on rodent cells. To investigate the reactive transformation of human astrocytes *in vivo*, we performed stereotaxic injections of either saline or recombinant human tumor necrosis factor-alpha (TNF α), a pro-inflammatory cytokine known to induce reactive astrogliosis^{1,37}, into the transplants, and performed fluorescence-activated cell sorting (FACS) to purify glial cells for single-cell RNA-seq (scRNA-seq) 5 h postinjection (Fig. 5a–c, Extended Data Fig. 9a,b and Supplementary Table 10). We found that DEGs associated with acute reactivity exhibited significant heterogeneity across astrocyte subpopulations (Fig. 5d,e and Extended Data Fig. 9c,d). Following TNF α treatment, we observed a significant expansion of cluster 2 astrocytes, which were identified by their expression of CD44, CD38 and GFAP (Fig. 5c,f). These reactive astrocytes were characterized by genes that have been previously linked to pro-inflammatory pathways and astrocyte pathogenic activities in neurotoxicity, such as the activation of nuclear factor kappa B (NF- κ B) and interferon pathways (Fig. 5g and Extended Data Fig. 9e). We also observed downregulation of genes involved in oxidative phosphorylation, NADH dehydrogenase complex assembly and mitochondrial respiratory chain complex assembly in cluster 2 astrocytes following TNF α treatment (Fig. 5g and Extended Data Fig. 9f). Taken together, our findings indicate that there is significant reactive heterogeneity across different human astrocyte subpopulations *in vivo*.

CD38 mediates inflammation-induced stresses in astrocytes

To gain further insights into the cellular changes that occur during human astrocyte reactivity, we treated glia-enriched cortical organoids with TNF α for 24 h and examined the inflammatory processes following the treatment (Fig. 6a,b and Extended Data Fig. 10a,b). Our results confirmed a rapid upregulation of pro-inflammatory cytokines, interferon signaling and the NF- κ B signaling pathway (Fig. 6b and Extended Data Fig. 10a,b). We also observed NF- κ B nuclear translocation in astrocytes (Fig. 6c). These results demonstrate that *in vitro* astrocytes can recapitulate the molecular changes *in vivo*.

Transcriptomics suggests dysregulation of metabolism and mitochondrial function in reactive astrocytes (Fig. 5g and Extended Data Fig. 9f). To investigate changes in NAD $^+$ metabolism and mitochondrial

function in reactive astrocytes, we purified GFAP::tdTomato $^+$ astrocytes from *in vitro* organoids (Fig. 6d and Extended Data Fig. 10c). Our analysis revealed reduced NAD $^+$ /NADH ratio (Fig. 6e) and glutathione (reduced to oxidized or GSH/GSSH) ratio (Fig. 6f) in astrocytes following TNF α treatment, suggesting metabolic stress and oxidative stress in reactive astrocytes. CD38 is a major regulator of NAD $^+$ levels, and a gradual increase in CD38 has been implicated in the decline of NAD $^+$ with age³⁹. We observed significant upregulation of CD38 in reactive astrocytes (Extended Data Fig. 10d). We next investigated whether CD38 mediated the reductive metabolic stress and oxidative stress. After treating human astrocytes with TNF α and a potent CD38 inhibitor 78c, we found significantly reduced metabolic and oxidative stress (Fig. 6e,f). Cellular stress and metabolic cues can cause the mitochondrial network to fragment, which then promotes mitophagy and is associated with cell death⁴⁰. Reactive astrocytes showed significant increases in mitochondrial fragmentation, which was markedly reduced by 78c (Fig. 6g,h). These results suggest a mechanism by which a major NADase CD38 mediates metabolic and mitochondrial dysregulation in reactive astrocytes.

Discussion

While brain organoid models have been useful for studying human neurodevelopment and neurological disorders, studies of astrocyte function in such models have remained limited. This is partly due to the late onset of gliogenesis in humans, which is recapitulated in cortical organoid models⁷. Prolonged culture of neural progenitor cells (NPCs) in media containing gliogenic factors^{12,13} or repeated passaging^{41,42} confers gliogenic competency but eliminates neurogenic potentials. In this study, we demonstrate that induction of a gliogenic switch by the addition of a gliogenic factor PDGF-AA and astrocyte-supporting medium for 3 weeks successfully enables accelerated astrogliogenesis in a substantial portion of cells while retaining the neurogenic potential for the majority of cells. In this context, our organoid model not only efficiently generates astrocytes in a time window comparable to previously reported 2D astrocyte differentiation protocols^{10–13} but also gives rise to other brain cell types, including cortical excitatory neurons, inhibitory neurons and oligodendrocyte progenitor cells (OPCs; Supplementary Fig. 1). Additionally, transcriptomic analysis

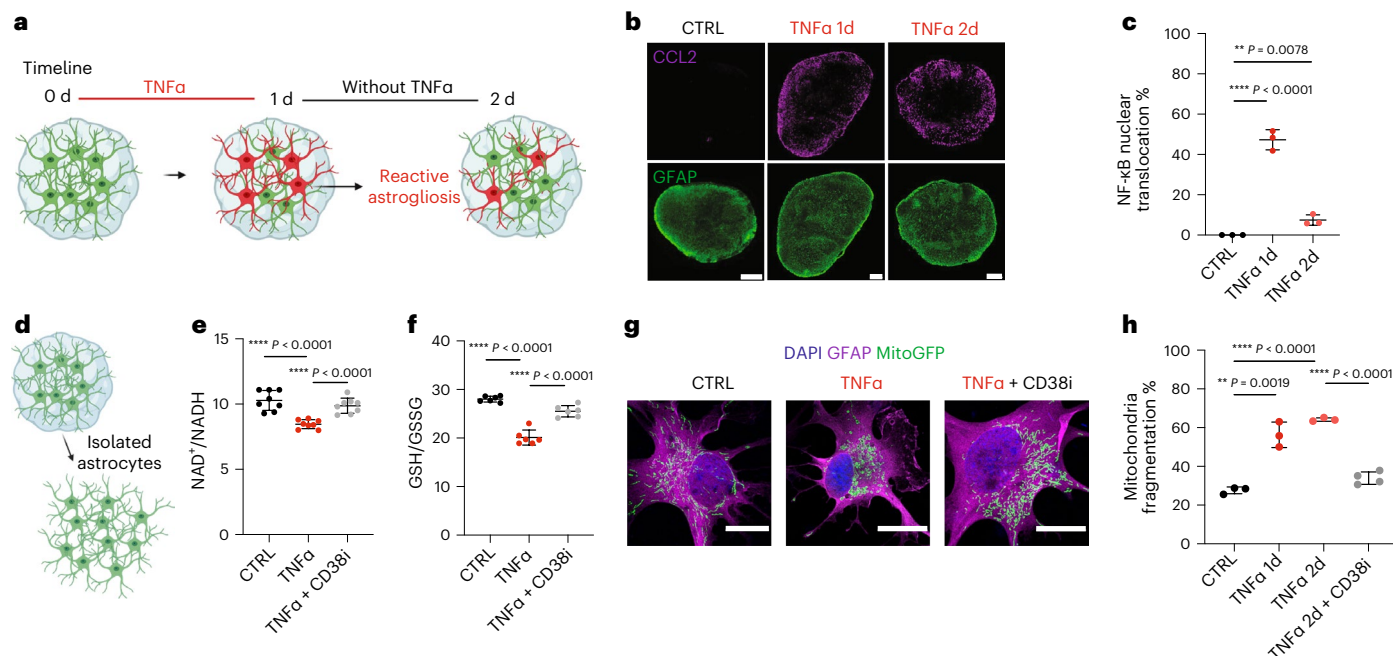


Fig. 6 | CD38 mediates inflammation-induced metabolic and mitochondrial stresses in human astrocytes. **a**, Schematic representation of the experimental design. **b**, Confocal images of in vitro 6-month-old glia-enriched cortical organoids at different time points (day 0, day 1 and day 2) post-TNF α treatment. Immunostaining for astrocytes (GFAP, green) and monocyte chemoattractant protein-1 (CCL2, magenta). Scale bars, 200 μ m. **c**, Quantification of the percentage of astrocytes with nuclear translocation of NF- κ B (three organoids per group). Each dot represents one organoid. Bars, mean \pm s.d. Two-sided t-test, **P = 0.0078, ***P < 0.0001. **d**, Schematic representation of astrocyte purification process from organoids. **e**, Dot plot showing the ratio of NAD $^+$ to NADH (n = 8 independent experiments per group). Each dot represents one independent experiment. Bars, mean \pm s.d. Two-sided t-test, ****P < 0.0001.

f, Dot plot showing the ratio of GSH to GSSG (n = 6 independent experiments per group). Each dot represents one independent experiment. Bars, mean \pm s.d. Two-sided t-test, ****P < 0.0001. **g**, Confocal images of astrocytes treated with saline, TNF α and TNF α together with CD38 inhibitor 78c. Immunostaining for astrocytes (GFAP::tdTomato, magenta) and mitochondria (mitoGFP, green). Scale bars, 10 μ m. **h**, Percentage of astrocytes with fragmented mitochondria (CTRL = 150 cells examined over three independent experiments; TNF α 1d = 150 cells examined over three independent experiments; TNF α 2d + CD38i = 200 cells examined over four independent experiments). Each dot represents one independent experiment. Bars, mean \pm s.d. Two-sided t-test, **P = 0.0019, ****P < 0.0001.

revealed that astrocytes generated in our model exhibit enhanced maturation compared to those derived from cortical organoids²¹ when transplanted into rodent cortices. Therefore, our organoid model provides an opportunity to study human astrocyte function in neurodevelopment and neurological diseases.

Human astrocytic complexity correlates with the increased functional competence of the adult human brain^{29,31}. In the human brain, astrocytes display a remarkable morphological diversity according to cortical layers and form anatomically defined subclasses^{29,31}. Although neonatal engraftment of human glial progenitor cells has allowed the progressive expansion of human glial cells in the host brain^{43–45}, to the best of our knowledge, it is still limited in fully reproducing the morphological complexity observed in the human brain. Notably, our model is capable of producing hominid-specific varicose astrocytes, a feature that was not observed in previous models. Our study has also uncovered the diversification of layer-specific expression patterns in astrocytes by spatial transcriptome profiling. Pial interlaminar astrocytes within the transplants expressed many astrocyte markers, including GFAP, S100B, CD44 and AQP4, and showed increased expression of GFAP, AQP4, ID1 and ID3 compared to cortical astrocytes, resembling the expression profiles of subpial astrocytes observed in mice^{46,47} and interlaminar astrocytes reported in humans^{48,49}. In contrast, cortical protoplasmic astrocytes displayed an upregulation of genes involved in regulating cholesterol biosynthesis, synapse formation and synaptic activity, while fibrous astrocytes expressed genes involved in the initiation of myelination. These findings contribute to our understanding of the unique molecular processes governing the spatial organization of astrocytes within the cortical architecture. Of note, the NanoString

GeoMx platform used in this study did not permit discrete identification of gene expression variations at single-cell resolution. This lack of single-cell resolution represents a notable constraint in our analysis, where ROIs, although enriched for SOX9, encompass various astrocytic types, thereby limiting our capacity to delineate transcriptional distinctions at a more refined morphological level.

Our model also provides a platform to study astrocyte function during neuroinflammation and disease progression. The previous notion of astrocyte reactivity being a uniform response to tissue damage has been challenged by accumulating evidence suggesting that astrocytes are a diverse population of cells^{36,50}. Our findings show that transcriptional changes associated with acute astrocyte reactivity in vivo are highly heterogeneous among human astrocyte subpopulations. We also demonstrate that metabolic and mitochondrial stresses induced by inflammation can be alleviated through inhibiting cyclase/hydrolase activity of CD38, a major NADase expressed in a subset of astrocytes and upregulated in response to TNF α treatment. This model thus presents a platform to interrogate cellular function under physiological conditions that is otherwise difficult to investigate in other models and for drug discovery to treat human brain diseases.

Online content

Any methods, additional references, Nature Portfolio reporting summaries, source data, extended data, supplementary information, acknowledgements, peer review information; details of author contributions and competing interests; and statements of data and code availability are available at <https://doi.org/10.1038/s41587-024-02157-8>.

References

1. Liddelow, S. A. et al. Neurotoxic reactive astrocytes are induced by activated microglia. *Nature* **541**, 481–487 (2017).
2. Qian, X., Song, H. & Ming, G. L. Brain organoids: advances, applications and challenges. *Development* **146**, dev166074 (2019).
3. Wang, M., Zhang, L. & Gage, F. H. Modeling neuropsychiatric disorders using human induced pluripotent stem cells. *Protein Cell* **11**, 45–59 (2020).
4. Lancaster, M. A. et al. Cerebral organoids model human brain development and microcephaly. *Nature* **501**, 373–379 (2013).
5. Kim, J., Koo, B. K. & Knoblich, J. A. Human organoids: model systems for human biology and medicine. *Nat. Rev. Mol. Cell Biol.* **21**, 571–584 (2020).
6. Velasco, S. et al. Individual brain organoids reproducibly form cell diversity of the human cerebral cortex. *Nature* **570**, 523–527 (2019).
7. Sloan, S. A. et al. Human astrocyte maturation captured in 3D cerebral cortical spheroids derived from pluripotent stem cells. *Neuron* **95**, 779–790 (2017).
8. Qian, X. et al. Sliced human cortical organoids for modeling distinct cortical layer formation. *Cell Stem Cell* **26**, 766–781 (2020).
9. Molofsky, A. V. et al. Astrocytes and disease: a neurodevelopmental perspective. *Genes Dev.* **26**, 891–907 (2012).
10. Tchieu, J. et al. NFIA is a gliogenic switch enabling rapid derivation of functional human astrocytes from pluripotent stem cells. *Nat. Biotechnol.* **37**, 267–275 (2019).
11. Canals, I. et al. Rapid and efficient induction of functional astrocytes from human pluripotent stem cells. *Nat. Methods* **15**, 693–696 (2018).
12. Santos, R. et al. Differentiation of inflammation-responsive astrocytes from glial progenitors generated from human induced pluripotent stem cells. *Stem Cell Reports* **8**, 1757–1769 (2017).
13. Barbar, L. et al. CD49f is a novel marker of functional and reactive human iPSC-derived astrocytes. *Neuron* **107**, 436–453 (2020).
14. Zhang, J. & Liu, Q. Cholesterol metabolism and homeostasis in the brain. *Protein Cell* **6**, 254–264 (2015).
15. Daneman, R. & Prat, A. The blood-brain barrier. *Cold Spring Harb. Perspect. Biol.* **7**, a020412 (2015).
16. Mansour, A. A. et al. An in vivo model of functional and vascularized human brain organoids. *Nat. Biotechnol.* **36**, 432–441 (2018).
17. Bao, Z. et al. Human cerebral organoid implantation alleviated the neurological deficits of traumatic brain injury in mice. *Oxid. Med. Cell. Longev.* **2021**, 6338722 (2021).
18. Daviaud, N., Friedel, R. H. & Zou, H. Vascularization and engraftment of transplanted human cerebral organoids in mouse cortex. *eNeuro* **5**, ENEURO.0219-18.2018 (2018).
19. Kitahara, T. et al. Axonal extensions along corticospinal tracts from transplanted human cerebral organoids. *Stem Cell Reports* **15**, 467–481 (2020).
20. Shi, Y. et al. Vascularized human cortical organoids (vOrganoids) model cortical development in vivo. *PLoS Biol.* **18**, e3000705 (2020).
21. Revah, O. et al. Maturation and circuit integration of transplanted human cortical organoids. *Nature* **610**, 319–326 (2022).
22. Jgamadze, D. et al. Structural and functional integration of human forebrain organoids with the injured adult rat visual system. *Cell Stem Cell* **30**, 137–152 (2023).
23. Qian, X. et al. Generation of human brain region-specific organoids using a miniaturized spinning bioreactor. *Nat. Protoc.* **13**, 565–580 (2018).
24. Qian, X. et al. Brain-region-specific organoids using mini-bioreactors for modeling ZIKV exposure. *Cell* **165**, 1238–1254 (2016).
25. Langfelder, P. & Horvath, S. WGCNA: an R package for weighted correlation network analysis. *BMC Bioinformatics* **9**, 559 (2008).
26. Morabito, S. et al. Single-nucleus chromatin accessibility and transcriptomic characterization of Alzheimer's disease. *Nat. Genet.* **53**, 1143–1155 (2021).
27. Allen, N. J. & Eroglu, C. Cell biology of astrocyte-synapse interactions. *Neuron* **96**, 697–708 (2017).
28. Stogsdill, J. A. et al. Astrocytic neurotrophins control astrocyte morphogenesis and synaptogenesis. *Nature* **551**, 192–197 (2017).
29. Oberheim, N. A. et al. Uniquely hominid features of adult human astrocytes. *J. Neurosci.* **29**, 3276–3287 (2009).
30. Zhang, Y. et al. Purification and characterization of progenitor and mature human astrocytes reveals transcriptional and functional differences with mouse. *Neuron* **89**, 37–53 (2016).
31. Oberheim, N. A., Wang, X., Goldman, S. & Nedergaard, M. Astrocytic complexity distinguishes the human brain. *Trends Neurosci.* **29**, 547–553 (2006).
32. Merritt, C. R. et al. Multiplex digital spatial profiling of proteins and RNA in fixed tissue. *Nat. Biotechnol.* **38**, 586–599 (2020).
33. Li, Y. et al. Direct labeling and visualization of blood vessels with lipophilic carbocyanine dye Dil. *Nat. Protoc.* **3**, 1703–1708 (2008).
34. Herring, C. A. et al. Human prefrontal cortex gene regulatory dynamics from gestation to adulthood at single-cell resolution. *Cell* **185**, 4428–4447 (2022).
35. Cao, J. et al. The single-cell transcriptional landscape of mammalian organogenesis. *Nature* **566**, 496–502 (2019).
36. Sofroniew, M. V. & Vinters, H. V. Astrocytes: biology and pathology. *Acta Neuropathol.* **119**, 7–35 (2010).
37. Zamani, J. L. et al. Genomic analysis of reactive astrogliosis. *J. Neurosci.* **32**, 6391–6410 (2012).
38. Anderson, M. A. et al. Astrocyte scar formation aids central nervous system axon regeneration. *Nature* **532**, 195–200 (2016).
39. Tarrago, M. G. et al. A potent and specific CD38 inhibitor ameliorates age-related metabolic dysfunction by reversing tissue NAD⁺ decline. *Cell Metab.* **27**, 1081–1095 e1010 (2018).
40. Sprenger, H. G. & Langer, T. The good and the bad of mitochondrial breakups. *Trends Cell Biol.* **29**, 888–900 (2019).
41. Krencik, R. & Zhang, S. C. Directed differentiation of functional astroglial subtypes from human pluripotent stem cells. *Nat. Protoc.* **6**, 1710–1717 (2011).
42. Palm, T. et al. Rapid and robust generation of long-term self-renewing human neural stem cells with the ability to generate mature astroglia. *Sci. Rep.* **5**, 16321 (2015).
43. Han, X. et al. Forebrain engraftment by human glial progenitor cells enhances synaptic plasticity and learning in adult mice. *Cell Stem Cell* **12**, 342–353 (2013).
44. Windrem, M. S. et al. A competitive advantage by neonatally engrafted human glial progenitors yields mice whose brains are chimeric for human glia. *J. Neurosci.* **34**, 16153–16161 (2014).
45. Mariani, J. N., Zou, L. & Goldman, S. A. Human glial chimeric mice to define the role of glial pathology in human disease. *Methods Mol. Biol.* **1936**, 311–331 (2019).
46. Zeisel, A. et al. Brain structure. Cell types in the mouse cortex and hippocampus revealed by single-cell RNA-seq. *Science* **347**, 1138–1142 (2015).
47. Bayraktar, O. A. et al. Astrocyte layers in the mammalian cerebral cortex revealed by a single-cell in situ transcriptomic map. *Nat. Neurosci.* **23**, 500–509 (2020).
48. Hodge, R. D. et al. Conserved cell types with divergent features in human versus mouse cortex. *Nature* **573**, 61–68 (2019).
49. Jorstad, N. L. et al. Transcriptomic cytoarchitecture reveals principles of human neocortex organization. *Science* **382**, eadf6812 (2023).
50. Burda, J. E. et al. Divergent transcriptional regulation of astrocyte reactivity across disorders. *Nature* **606**, 557–564 (2022).

Publisher's note Springer Nature remains neutral with regard to jurisdictional claims in published maps and institutional affiliations.

Springer Nature or its licensor (e.g. a society or other partner) holds exclusive rights to this article under a publishing agreement with the author(s) or other rightsholder(s); author

self-archiving of the accepted manuscript version of this article is solely governed by the terms of such publishing agreement and applicable law.

© The Author(s), under exclusive licence to Springer Nature America, Inc. 2024

Methods

Human PSCs

Human embryonic stem cells (hESCs) Hues6 (National Institutes of Health (NIH)-approved ESC line, obtained from HSCI iPS Core)⁵¹, H9 (Wisconsin International Stem Cell bank, WiCell Research Institute, WA09 cells)⁵² and hiPSCs 822 were used in the current study. H9 cells were transduced with pCSC-CAG-GFP lentiviruses, and GFP-expressing cells were FACS-sorted as previously described¹⁶. Protocols were previously approved by the Salk Institutional Review Board, and informed consent was obtained from the subjects.

Mice

All animal experiments described in the current study were approved by the Institutional Animal Care and Use Committee at the Salk Institute for Biological Studies (12-00022) and were conducted in compliance with the NIH's Guide for the Care and Use of Laboratory Animals. Immune-deficient mice NOD.Cg-*Prkdc*^{scid} *Il2rg*^{tm1Wjl}/SzJ (Jackson Laboratory, 005557) were generated in our lab by breeding and kept on a 12-h light/12-h dark cycle in a housing group of 2–5 mice in each cage. Male and female mice 6–12 weeks of age were randomly used in this study.

Human PSC culture

Human PSCs were cultured as previously described^{16,53}. PSC colonies were maintained on Matrigel-coated six-well plates (Matrigel; Corning, 354277; hESC-Qualified) using mTeSR Plus (STEMCELL Technologies, 85850) and were incubated in a 5% CO₂ humidified atmosphere at 37 °C. PSC colonies were passaged at a ratio of 1:6 every 3–6 d using ReLeSR (STEMCELL Technologies, 5872). All human PSCs were maintained in feeder-free culture conditions for 20–40 generations and confirmed negative for mycoplasma. Cells were confirmed normal with karyotyping. All experiments involving cells from human subjects were performed in compliance with the institutional Embryonic Stem Cell Research Oversight Committee.

Generation of glia-enriched cortical organoids

To generate embryoid bodies, intact PSC colonies were treated with 1 mg ml⁻¹ Collagenase type IV (Invitrogen, 17104-019) for 20–45 min at 37 °C and mechanically detached with a cell scraper. Dissociated colonies were maintained in an ultra-low-attachment dish (Nunc) under stationary conditions for 2 d and were fed with mTeSR Plus supplemented with 10 mM ROCK inhibitor Y-27632 (Tocris Bioscience, 1254). From day 1, cells were maintained in astrocyte medium (AstroM; ScienCell, 1800) supplemented with astrocyte growth supplement (AGS; ScienCell, 1800), 2% FBS, 500 ng ml⁻¹ Noggin (R&D Systems, 6057-NG), 10 ng ml⁻¹ PDGF-AA (Proteintech, HZ-1215) and 1× 2-mercaptoethanol (Gibco, 21985032) until day 14. On day 15, organoids (10–12 organoids in each well of six-well ultra-low-attachment plates) were transferred onto an orbital shaker (75 r.p.m.) and maintained in AM supplemented with AGS, 10 ng ml⁻¹ PDGF-AA and 1× 2-mercaptoethanol for an additional week. From day 22, organoids were maintained on orbital shaker (75 r.p.m.) in medium consisting of DMEM/F-12 with Glutamax (Thermo Fisher Scientific, 10565018), 1× N2 supplement (Thermo Fisher Scientific, 17502-048), 1× B27 (without RA; Thermo Fisher Scientific, 12587010), 1× MEM-NEAA (Thermo Fisher Scientific, 11140050), 10% FBS (Omega Scientific, FB-01; lot 991851) and 1× 2-mercaptoethanol. Organoids cultured beyond day 60 were additionally supplemented with 20 ng ml⁻¹ brain-derived neurotrophic factor (BDNF; R&D Systems, 248-BDB), 20 ng ml⁻¹ glial cell line-derived neurotrophic factor (GDNF; R&D Systems, 212-GD), 0.2 mM ascorbic acid (AA; STEMCELL Technologies, 72132) and 0.5 mM cyclic adenosine monophosphate (cAMP; Tocris Bioscience, 1141). All media changes were done every other day. All organoids for transplantation experiments were preselected for the development of organized neuroepithelium budding and the absence of cyst formation. In addition, organoids from the same culture batch were examined by immunostaining for verification of neuronal and glial differentiation.

Intracerebral implantation of glia-enriched cortical organoids

Organoid implantations were performed as previously described¹⁶. Glia-enriched organoids were cultured in vitro for 8–10 weeks before implantation. Mice were anesthetized with 3–5% isoflurane inhalation for induction and 1–2% isoflurane for maintenance. Each animal was fixed onto a stereotaxic frame for the duration of all surgical procedures with body temperatures maintained at 37 °C using a water-circulation heating pad (Gaymar Industries). Dexamethasone (2.5 mg kg⁻¹) was injected subcutaneously to minimize edema. Upon the removal of the skin above the scalp, a ~3 mm diameter craniotomy was performed by drilling into the skull. The underlying dura mater was subsequently removed with forceps. A unilateral lesion was created in the region of the retrosplenial cortex through aspiration with a blunt-tip needle attached to a vacuum line. The brain tissue overlying the anterior colliculus was removed, and the vascular bed of the choroidal fissure was exposed. Sterile saline and a piece of Gelfoam (Pfizer) were used to prevent excessive bleeding. The organoid transplant was placed into the cavity dorsal to the hippocampus. Upon transplantation, the organoid was sealed with a 5-mm glass coverslip using adhesive glue and the wound was secured with dental cement (Stoeling)⁵⁴. Upon completion of the surgery, carprofen (5 mg kg⁻¹, i.p., 100 µl of 1 mg ml⁻¹) and Buprenorphine SR-Lab (1.0 mg kg⁻¹, subcutaneous) were administered to minimize inflammation and pain. The mice were then returned to their home cages for recovery on a heating pad.

Stereotaxic injection

Mice were anesthetized with 3–5% isoflurane via inhalation for induction and 1–2% isoflurane for maintenance. Each mouse was fixed onto a stereotaxic frame for the duration of all surgical procedures with body temperatures maintained at 37 °C using a water-circulation heating pad (Gaymar Industries). For direct TNFα injection into brain organoids, the preexisting dental cement and cranial window were removed first, followed by injection of 1 µl of 250 ng of recombinant human TNFα (Sino Biological, 10602-HNAE) or saline at a speed of 1 µl per minute using a Hamilton syringe. The 1 µl injection volume was split across two different Z locations. After the injection was completed, the needle was retracted at a rate of 0.2–0.5 mm per minute. A new cranial window was placed using adhesive glue and secured with dental cement (Stoeling). Buprenorphine SR-Lab (1.0 mg kg⁻¹, subcutaneous) was administered to minimize postoperative pain. The mice were immediately placed on a warm heating pad until recovery.

Virus transduction

pBOB-GFAP-tdTomato lentiviral vector was obtained from the lab of I. Verma at the Salk Institute. Lentiviruses were produced by the virus core at Salk Institute. To transduce organoids, 1 µl of lentivirus (titer was 10¹² genome copies per ml (GC ml⁻¹)) was added in each well of a six-well plate containing 3 ml medium and 4–6 organoids. Virus-containing medium was completely changed after 2 d.

pAAV.GFAP.eGFP.WPRE.hGH AAV5 viral prep was a gift from J.M. Wilson (Addgene viral prep 105549-AAV5; RRID: Addgene_105549 with a titer of 10¹³ GC ml⁻¹). AAV particles were injected into the mouse brain to visualize human and mouse astrocytes. Briefly, a mouse with an organoid implant was anesthetized with isoflurane (5% for induction and 2% for maintenance). The mouse was fixed on the stereotaxic instrument and the glass coverslip covering the implant was drilled through. One microliter AAV5 virus was slowly injected into the organoid transplant for a duration of 5 min. The mice were allowed to recover on a heating pad and returned to their home cages.

Histological processing

In vitro cultured organoids were fixed in 4% paraformaldehyde (PFA) for 45–60 min followed by three washings with PBS. Organoids were then transferred to 30% sucrose solution at 4 °C overnight. Four to six

organoids were transferred into blocks in a tissue-freezing medium, frozen on dry ice and stored at -80 °C.

To obtain brain tissues containing organoid implants, the mice were first deeply anesthetized with ketamine/xylazine (130 mg kg⁻¹, 15 mg kg⁻¹; i.p.) and then subjected to transcardial perfusion of 15 ml ice saline followed by 15 ml 4% PFA. The brains were subsequently dissected out and transferred into 15-ml conical tubes containing 4% PFA for postfixation overnight at 4 °C. Brains were cryoprotected for 48–72 h in 30% sucrose with 0.05% NaN₃ at 4 °C. Each brain was trimmed coronally and embedded in a tissue-freezing medium (General Data).

All blocks were left to equilibrate to the temperature of the cryostat ~30 min before sectioning. Thirty 40-μm cryosections of organoids were obtained using a cryostat (Leica), mounted on Superfrost plus slides (Thermo Fisher Scientific, Menzel-Glaser), dried at room temperature for 30 min and stored at -20 °C. For each section set, one section was collected onto a slide to obtain a total of 20 slides, and this collection method was repeated until tissue was exhausted.

Immunohistochemistry and imaging acquisition

Immunofluorescence staining was performed with thawed slides, with the tissue area and slide edges outlined using a hydrophobic PAP pen. The slides were washed three times with PBS and blocked and permeabilized in blocking solution (5% normal donkey serum, 0.1% Triton X-100 in PBS) in a humidified chamber for 1 h at room temperature. Organoid slides were incubated with primary antibodies diluted in the blocking solution at 4 °C overnight. Primary antibodies used were rabbit anti-NFIA (Abcam, ab41851; 1:250), rat anti-SOX2 (clone Btjce; Invitrogen, 14-9811-82; 1:400), rabbit anti-GFAP (Dako Z0334; 1:500), chicken anti-GFAP (EMD Millipore, AB5541; 1:1,000), chicken anti-GFP (Aves Labs, GFP-1020; 1:1,000), mouse anti-hGFAP (clone number not provided by the vendor; TaKaRa, Y40420; 1:500), mouse anti-human nuclear antigen (HuNu; clone 235-1; Abcam, ab215755; 1:250), rabbit anti-NeuN (EMD Millipore, ABN78; 1:250), rat anti-Ly6C (Clone ER-MP20; Abcam, ab15627; 1:500), rabbit anti-AQP4 (Alomone Labs, AQP-004; 1:400), rabbit anti-Kir4.1 (Alomone Labs, APC-035; 1:250), rabbit anti-glucose transporter GLUT1 (Abcam, ab115730; 1:100), rabbit anti-tdTomato (Rockland, 600-401-379; 1:500), rabbit anti-laminin (Novus a biotechne brand, NB300-144SS; 1:500), mouse anti-hHepaCAM (clone 419305; R&D Systems, MAB4108; 1:400), rabbit anti-S100B (Abcam, ab52642; 1:1,000), rabbit anti-TBR2/Eomes (Abcam, ab275960; 1:250), rat anti-CTIP2 (clone 25B6; Abcam, ab18465; 1:200), rabbit anti-SATB2 (Abcam, ab92446; 1:100), mouse anti-HOPX (clone E-1; Santa Cruz Biotechnology, sc-398703; 1:200), rabbit anti-NG2 (EMD Millipore, AB5320; 1:200), goat anti-CD31 (R&D Systems, AF3628; 1:500), rabbit anti-IBA1 (Wako, 019-19741; 1:400), goat anti-IBA1 (Abcam, ab48004; 1:400), mouse anti-SV2 (clone number not provided by the vendor, DSHB, SV2-c; 1:500), rabbit anti-PSD95 (Invitrogen, 51-6900; 1:250), rabbit anti-myelin basic protein (Abcam, ab218011; 1:400), rat anti-CD44 (clone IM7.8.1R; R&D Systems, MAB6127; 1:500), mouse anti-EAAT2 (clone E-1, Santa Cruz Biotechnology, sc-365634; 1:250), goat anti-hSPARC-like 1 (HEVIN; R&D Systems, AF2728; 1:50), rabbit anti-PDGFRα (Abcam, ab203491; 1:200), mouse anti-hCD38 (clone 240742; R&D Systems, MAB2404; 1:200), rabbit anti-CXCL10/IP10 (Invitrogen, MA5-32674; 1:200), rabbit anti-CCL2/MCP-1 (Novus a biotechne brand, NBP1-07035; 1:100) and rabbit anti-connexin 43 (Cell Signaling Technology, 3512S; 1:200). After three washes with PBS, slides were incubated with the appropriate fluorochrome-conjugated secondary antibodies diluted in blocking solution at room temperature for 1 h in the dark. Alexa Fluor secondary antibodies (Jackson ImmunoResearch) diluted in a blocking solution at 1:250 were used. Finally, all slides were counterstained with DAPI (Sigma-Aldrich, D9542; 1 μg ml⁻¹) for 5 min, rinsed three times in PBS before mounting with mounting solution (ProLong gold, Thermo Fisher Scientific) and left to dry for at least 48 h at room temperature before imaging acquisition. Slides were stored at 4 °C.

All images were acquired on a Zeiss LSM880 confocal microscope, Olympus VS-120 Virtual Slide Scanning Microscope (Olympus), or Revolve (ECHO), and processed with Zen software (Zeiss) and ImageJ software (NIH).

NanoString GeoMx Digital Spatial Profiler

FFPE tissue from a mouse brain with a human organoid transplant was sectioned at 5 μm and mounted onto positively charged slides with four sections per slide; subsequently, it was profiled using a NanoString GeoMx Digital Spatial Profiler (DSP) (NanoString Technologies) as previously described³². The NanoString commercial Human Whole Transcriptome Atlas (GeoMx Hu WTA) panel (>18,000 protein-coding genes) was selected. Tissue morphology was visualized using fluorescent-conjugated hGFAP Alexa Fluor 594 (STEMI23; TaKaRa; conjugated using Lightning-Link Rapid Alexa Fluor 594 Antibody Labeling Kit; 8 μg ml⁻¹), SOX9 Alexa Fluor-647 (clone EPR14335; Abcam, ab196184; 8 μg ml⁻¹) and SYTO-13 to detect nucleic acids. The slide was scanned on a NanoString GeoMx DSP platform, and individual ROIs with a maximum diameter of 660 μm were created. Once each ROI was compartmentalized, cell segmentation was performed to identify SOX9⁺/CYTO-13⁺ cells for subsequent ultraviolet-cleaved indexing oligonucleotides collection into a 96-well plate. Libraries were prepared according to the manufacturer's instructions (protocol MAN-10153-03). Samples were sequenced on the Illumina MiniSeq platform (MiniSeq High Output Kit PE 75 cycles), and reads were digitally quantified and normalized using GeoMx DSP Data Analysis Suite 3.0 (NanoString Technologies) following the manufacturer's instructions³². Target filtering was applied to retain gene targets with read counts above the limit of quantification (defined as geomean (NegProbe) × geoSD (NegProbe)² for each ROI) in at least 10% of ROIs. Q3 normalization was applied to the filtered ROIs and gene targets. The ROIs were categorized according to the spatial groups for subsequent analysis. Differential gene expression across groups was analyzed using a linear mixed effect model followed by the Benjamini–Hochberg multiple correction test. DEGs were defined as fold change (FC) >1.5 or <-1.5, and adjusted *P* < 0.05. The parameters chosen for GSEA included a minimum coverage of 20% of genes within the pathway and a pathway size between 15 and 500 genes, using Reactome Version Build 78+ NCBI_08122021.

Cytokine stimulation in vitro

Organoids or purified astrocytes were treated with 50 ng ml⁻¹ recombinant human TNFα (Sino Biological, 10602-HNAE) or PBS (vehicle) for 24 h in maturation media. After washing with PBS, the samples were changed to fresh maturation media. To assess the effect of CD38 inhibition, samples were treated with 0.5 μM 78c (Tocris Bioscience, 6391) and 50 ng ml⁻¹ TNFα for 24 h in maturation media, followed by 0.5 μM 78c for an additional 24 h.

Mitochondrial morphological analysis

Purified astrocytes were transduced with a lentiviral vector encoding MitoEGFP under the CAG promoter. Cells were fixed in 4% PFA for 10 min, washed three times with PBS and subjected to immunohistochemistry and imaging acquisition. The EGFP signal (MitoEGFP) was used to analyze the mitochondrial shape in ImageJ (NIH).

Functional assays

Reduced (GSH) and oxidized (GSSG) glutathione contents were assessed in astrocytes using the GSH/GSSG-Glo assay kit (Promega, V6611). The results are expressed as GSH/GSSG ratio. The NAD⁺/NADH ratio was assessed in cultured astrocytes using the NAD-Glo assay kit (Promega, G9071).

Glutamate uptake assay

Astrocytes purified from three iPSC lines of 5-month-old organoids and cultured NPCs were incubated in Hank's balanced salt solution (HBSS)

buffer without calcium and magnesium (Gibco) for 30 min, followed by incubation for 2 h in HBSS containing calcium and magnesium (Gibco) supplemented with 100 μ M glutamate. After 2 h, the media were collected and analyzed using a bioluminescent assay kit (Promega, Glutamate-Glo Assay, J7021) according to the manufacturer's instructions. Six to eight technical replicates per line were used.

Sholl analysis

GFAP::GFP AAV-transduced astrocytes from 3- and 5-month-old glia-enriched cortical organoids were stained with an antibody against GFP and imaged using a Zeiss LSM880 confocal microscope at $\times 63$ magnification with z-stack images. Images were opened in ImageJ, and a maximum intensity projection was performed. Astrocyte tracing was done manually using Simple Neurite Tracer tool⁵⁵. Sholl analysis was carried out through Simple Neurite Tracer with radial intervals of 1.26732 μ m.

qPCR

Total RNA was purified from organoids or astrocytes with a Direct-zol RNA Purification Kit (Zymo Research, R2061), according to the manufacturer's instructions. cDNA was synthesized using the SuperScript III First-Strand Synthesis System (Invitrogen). Quantitative PCR was performed using SYBR Green PCR Master Mix (Applied Biosystems) on a BioRad CFX384 thermal cycler. The relative mRNA abundance of target genes was normalized to that of GAPDH mRNA obtained in the same sample. The primer sequences are shown in Supplementary Table 11.

EM

A mouse with an implanted organoid was perfused and processed for EM as described elsewhere⁵⁶ with some modifications. The mouse was first anesthetized with ketamine/xylazine (130 mg kg⁻¹, 15 mg kg⁻¹; i.p.) and perfused with 25 ml of warm oxygenated Ringers solution, followed by 15 ml of warm buffered fixative (2.5% glutaraldehyde, 2% PFA, 3 mM CaCl₂ and 0.15 M sodium cacodylate) with Dil added to the solution to fluorescently label vasculature as previously described³³. The brain was carefully extracted from the skull and stored overnight at 4 °C in a fresh fixative solution. The following day, the brain was thoroughly rinsed with buffer (3 mM CaCl₂ and 0.15 M sodium cacodylate) and 120- μ m thick sections containing the organoid were collected using a vibrating blade microtome (Leica VT1000 S) with a bath of ice-cold buffer. Brain sections were serially rinsed with ice-cold buffer, followed by a rinse with ice-cold buffer containing 50 mM glycine. Sections were immersed in a shallow dish filled with ice-cold buffer and photographed using a dissecting microscope equipped with a camera (Olympus). Low-resolution confocal imaging was performed for GFP and Dil. A small rectangle was microdissected from the center of the organoid for serial section SEM. Sections used for SEM were left intact for processing. Samples were processed for high contrast with heavy metals as described elsewhere⁵⁷. Briefly, sections were immersed in buffered reduced osmium (1.5% osmium tetroxide, 1.5% potassium ferrocyanide, 3 mM CaCl₂ and 0.15 M sodium cacodylate) for 45 min in the dark at room temperature. Samples were then serially rinsed with ice-cold distilled water before 30 min of treatment with filtered 1% aqueous thiocarbohydrazide that was prepared at 60 °C for an hour before use. Samples were serially rinsed with ice-cold distilled water before amplifying staining with 1.5% aqueous osmium tetroxide for 45 min in the dark at room temperature. Sections to be imaged by SEM were set aside at this point for serial dehydration and critical point drying (Leica CPD300). The remaining microdissected samples were serially rinsed with ice-cold water before staining overnight with 1% uranyl acetate at 4 °C. The next day, samples were thoroughly rinsed with room-temperature distilled water and stained with Walton's lead aspartate for 30 min at 60 °C. Samples were rinsed again with room-temperature distilled water and serially dehydrated in ice-cold ethanol. Samples were then rinsed three times in anhydrous ethanol

before serial infiltration with Eponate 12 resin (hard formulation) over the course of 2 d and finally embedded in capsules for polymerization in a small oven for 3 d at 60 °C.

A ribbon of ~100 serial ultrathin sections was collected, and each section of approximate dimensions of 150 μ m–400 μ m–70 nm (x – y – z) was collected onto a silicon chip using Diatome diamond knives mounted on a Leica UC7 ultramicrotome as described elsewhere⁵⁸. The chip was mounted on an aluminum stub using carbon sticky tape and loaded into a Zeiss Sigma VP scanning EM equipped with a Gatan backscattered electron detector and both SmartSEM (Zeiss) and Atlas5 (Fibics) control software. An ROI near the center of the organoid implant was identified, and images were acquired with an accelerating voltage of 1.5 kV, a 20- μ m aperture, at a working distance of 9 mm. A multi-resolution map of a central section was acquired, identifying candidate blood vessels for further 3D analysis. Contiguous high-resolution images (8–8–70 nm per voxel, x – y – z) of a representative ROI containing a blood vessel were assembled into a series of 8-bit tiff files. Serial images were aligned using AlignEM-SWIFT to form a continuous 3D representation of the tissue volume.

Endothelial cell processes, pericyte and astrocyte processes contacting the blood vessel as well as tight junctions and basement membrane were identified by their ultrastructural characteristics and annotated using VAST Lite software. Cells and nuclei were exported using the VAST Lite Matlab toolkit as .obj files, which were imported into Blender software equipped with GAMer and Neuromorph add-ons. Object meshes were processed with GAMer to optimize geometry for visualization, before superimposition with three-dimensional electron microscopy (3DEM) data using Neuromorph. In this fashion, data were interrogated and rendered scenes and animations were produced using Blender. For video figures, rendered scenes were assembled into .avi files using ImageJ, postprocessed using After Effects (Adobe) and compressed using Handbrake (<https://handbrake.fr/>).

Dissociation of brain organoids and snRNA-seq

Nuclei extraction from fresh dissected *in vivo* brain organoids was performed according to a demonstrated protocol CG000124 (Rev E, nuclei isolation from cell suspensions and tissues for scRNA-seq) from 10x Genomics with minor modification. Briefly, freshly dissected *in vivo* brain organoids were pooled and lysed using a Dounce homogenizer in 1 ml of freshly prepared cold lysis buffer (Tris-HCl 10 mM (pH 7.4), NaCl 10 mM, MgCl₂ 3 mM, NP-40 0.1% in nucleus free water). Nuclei were centrifuged at 500g for 8 min and supernatant was discarded. Nuclei were then resuspended in freshly prepared cold nuclei wash and resuspension buffer (PBS, 1% BSA, RNase inhibitor 0.2 U μ l⁻¹) and filtered through a 35- μ m strainer (Corning). Nuclei were centrifuged at 500g for 5 min and resuspended again in nuclei wash and resuspension buffer for a total of two washes. After the second wash, nuclei were resuspended in ice-cold nuclei wash and resuspension buffer at a concentration of 800–1,200 cells per μ l, and ~17,400 cells per channel (to give an estimated recovery of 10,000 cells per channel) were loaded onto a Chromium Next GEM Chip G (10x Genomics) and processed through the Chromium Controller to generate single-cell gel beads in emulsion (GEMs). snRNA-seq libraries were prepared with the Chromium Next GEM Single Cell 3' GEM Library & Gel Bead Kit v.3.1 (10x Genomics) as per the manufacturer's instruction. Libraries from different samples were pooled, and 20,000 reads per nucleus were sequenced on a NovaSeq6000 (Illumina) or a NextSeq (Illumina) with 28 bases for read 1, 91 bases for read 2 and 8 bases for index 1.

Dissociation of organoid transplants and scRNA-seq

Single-cell dissociation from fresh dissected *in vivo* brain organoids was performed using the Neural Tissue Dissociation Kit (Miltenyi Biotech, 130-092-628) as per the manufacturer's instruction. Red blood cells were lysed with Red Blood Cell Lysis Solution (Miltenyi Biotech, 130-094-183) for 3 min, washed with 0.1% BSA in 1× PBS and prepared

for downstream applications. Cells were stained with PE anti-GLAST antibody (Miltenyi Biotec, 130-118-483; 1:50) for 30–40 min in the dark on ice, washed with PBS and resuspended in 0.1% BSA in 1× PBS. Cells were incubated with DAPI before sorting. After sorting, cells were resuspended in ice-cold PBS at a concentration of 500–1,200 cells per μ l and subjected to single-cell sequencing (10x Genomics) as described above.

sn/scRNA-seq data analysis

The Cell Ranger 6.0.1 pipeline (10x Genomics) was used to align reads from RNA-seq to the 10 \times hg19 human reference genome v1.2.0 and 10 \times mm10 mouse reference genome v1.2.0 and produce the associated cell-by-gene count matrix for the organoid transplants. The Cell Ranger 6.0.1 pipeline (10x Genomics) was used to align reads from RNA-seq to the 10 \times hg19 human reference genome v1.2.0 and produce the associated cell-by-gene count matrix for the *in vitro* organoids. Default parameters were used, except for -include-introns argument for nuclei samples. Unique molecular identifier counts were analyzed using the Seurat R package (v.4.0.1)⁵⁹. Human cells or nuclei (defined as nuclei with >95% genes mapped to hg19) were kept for subsequent analysis. Nuclei with <1% of mitochondrial contamination and between 500 and 6,000 expressed genes were retained for further analysis. Cells with <20% mitochondrial contamination and between 500 and 6,000 expressed genes were retained for further analysis. To prepare for integration, SCTransform was performed, and the top 3,000 features were used to find integration anchors. Integration was performed using the SCT normalized method. PCA was performed on the scaled data for the variable genes, and the top 30 principal components were implemented for the unsupervised clustering. Cells were clustered in PCA space using the FindNeighbors function (top 30 principal components) and the FindClusters function. Variation in the cells was visualized by UMAP.

DEGs were defined as genes significantly expressed (P adjusted for multiple comparisons <0.05) in ≥25% of cell populations with >0.25-fold difference (log scale) between groups of nuclei. DEGs between clusters of astrocytes before and post-TNF α treatment were identified as genes significantly expressed (P adjusted for multiple comparisons <0.05) with >0.25-fold difference (log scale). Visualization of intersecting genes was plotted using UpSetR (v1.4.0)⁶⁰. Gene Ontology (GO) terms of DEGs were represented using a maximum of 100 genes (Wilcoxon test, P <0.05, log(FC)>0.25) using the Enrichr⁶¹ database 'GO_Biological_Process_2021'.

Cluster correlation

For both 8-month-old organoid transplant and integrated snRNA-seq datasets, marker genes in each cluster were identified using FindAllMarkers() in Seurat, requiring to be detected in at least 25% of cells with log FC larger than 0.25. The top 50 marker genes from each cluster were selected by FC expression for the correlation analysis. The expression of top markers was averaged across cells within each cluster of our dataset and each annotated cell type in reference human brain dataset across six cortical areas from Allen Brain Atlas⁴⁸. The Pearson correlation coefficient between our dataset and the reference was calculated across clusters and presented in heatmap.

Module expression analysis

To calculate the differential expression of modules, the AddModuleScore function from Seurat was applied using the top 50 expressed genes from the upregulated mature astrocyte gene list curated from ref. 30. Two-sided Wilcoxon test was applied to compare the module scores in astrocytes from different time points, using the stats R package.

Weight gene co-expression network analysis

To learn patterns of coordinated gene regulation across the cells, we applied scWGCNA (v0.0.0.9000)²⁶ to several datasets. We selected

genes expressed in at least 5% of cells for downstream analysis. To construct the metacell gene expression matrix, the K-nearest neighbors (KNN) algorithm was used to identify groups of similar cells, and then the average expression of these cells was computed using the MetacellsByGroups function. For 10-week-old organoids and 8-month-old transplants, during metacell computation, we pooled 50 cells within the same cell type per cell line to retain the metadata for scWGCNA. For the integrated datasets, we pooled 25 cells within the same cell type for each time point. We then set up the expression matrix for the cell type of interest. To pick an adequate power for each dataset, we used the TestSoftPowers function to test values from 1 to 30. We next constructed a co-expression network with the selected soft power. To compute the harmonized module eigengenes, the ScaleData function was performed to regress variable features including 'nFeature_RNA' and 'percent.mt', and module eigengenes were calculated using the ModuleEigengenes function. Default parameter was used to compute module connectivity. To compute the hub gene signature score, the top 25 hub genes by eigengene-based connectivity were used. GO terms of each module were analyzed using the top 100 hub genes using the Enrichr⁶¹ database 'GO_Biological_Process_2021'.

Pseudotime analysis

To prepare cells for pseudotime analysis, the unknown cluster was first removed and the samples were re-integrated using the SCT method in Seurat. PCA was then calculated, and the top 30 principal components were used for UMAP visualization. Pseudotime analysis was performed using the Monocle 3 v1.0.0 software package³⁵ with the default parameters. The cells were subset to contain an equal amount from different time points. A starting point for the trajectory was chosen manually by finding an endpoint for the earliest developmental cell type. To test cell distribution along the trajectory, a one-sided Kolmogorov-Smirnov test was applied comparing the distribution of pseudotime values of cells from different time points, using the stats R package.

Cell type and age prediction

Cell type prediction was carried out with the Seurat package (v4.2.0), with the published integrated dataset as reference⁵⁹. The reference dataset was projected onto our query data based on the anchors identified by the FindTransferAnchors function, and the label of the cell type was predicted using the TransferData function. Cells that were not assigned with any reference labels were defined as 'Undetermined'. The original annotation and prediction labels were presented in the original UMAP space. The concordance between the original annotation and prediction was measured by calculating the assignment percentage of every type of annotated cell to the reference labels, which were then displayed in a heatmap.

For age prediction, our data were integrated with the reference age dataset³⁴ using the CCA merge method in Seurat⁵⁹. Within the integrated UMAP space, a KNN regression was carried out using the knn.reg function from the FNN R package (v1.1.3) with ten nearest neighbors. Cell ages were estimated from the arcsinh transformation of the reference ages, taking the mean of its neighbors. The age distribution among different groups was compared using the Wilcoxon rank-sum test.

Enrichment analyses

Gene set enrichment analyses of Hallmark gene sets and GO terms were performed with WebGestaltR package (v0.4.4) with a false discovery rate (FDR) <0.05 as the significance threshold, protein-coding genes as the reference list, a minimum number of genes in a category of 5 and permutation time of 1,000 (ref. 62). To prepare the input ranked gene list for GSEA, differential expression analyses were performed between two conditions using the FindMarkers function from Seurat. Genes were scored and ordered by the resulting P values and FCs.

Statistics and reproducibility

Statistical analyses were conducted using GraphPad Prism 9 and R (v4.1.2). Exact statistical values are presented in the figures and the source data. The data presented from representative experiments were independently replicated at least three times with similar outcomes, unless explicitly indicated by the sample size noted in each figure or Method section. This includes all microscopy data and quantitative PCR data.

Reporting summary

Further information on research design is available in the Nature Portfolio Reporting Summary linked to this article.

Data availability

snRNA-seq data are available in Gene Expression Omnibus (GEO) under the accession [GSE185472](#). The following public datasets were used for snRNA-seq analysis: Allen Brain Institute human adult snRNA-seq data from multiple cortical areas (<https://portal.brain-map.org/atlas-and-data/rnaseq/human-multiple-cortical-areas-smart-seq>; accessed October 2022), snRNA-seq data from broad temporal coverage from fetal to adulthood stages of the Brodmann area 8, 9, 10 and 46 prefrontal cortex regions (GEO accession [GSE168408](#)) and snRNA-seq from 8-month-old cortical organoid transplants (GEO accession [GSE190815](#)). For single-nucleus analysis, we used hg19 human reference genome v1.2.0 and mm10 mouse reference genome v1.2.0 provided by 10x Genomics. The sequences and gene files used to build the references can be achieved at ftp://ftp.ensembl.org/pub/grch37/release-84/fasta/homo_sapiens/dna/ and ftp://ftp.ensembl.org/pub/grch37/release-84/gtf/homo_sapiens/ (for human hg19 genome); ftp://ftp.ensembl.org/pub/release-84/fasta/mus_musculus/dna/ and ftp://ftp.ensembl.org/pub/release-84/gtf/mus_musculus/ (for mouse mm10 genome). All other raw data used for plotting in the figures are provided as source data. Source data are provided with this paper.

References

51. Cowan, C. A. et al. Derivation of embryonic stem-cell lines from human blastocysts. *New Engl. J. Med.* **350**, 1353–1356 (2004).
52. Thomson, J. A. et al. Embryonic stem cell lines derived from human blastocysts. *Science* **282**, 1145–1147 (1998).
53. Mertens, J. et al. Differential responses to lithium in hyperexcitable neurons from patients with bipolar disorder. *Nature* **527**, 95–99 (2015).
54. Goncalves, J. T. et al. In vivo imaging of dendritic pruning in dentate granule cells. *Nat. Neurosci.* **19**, 788–791 (2016).
55. Longair, M. H., Baker, D. A. & Armstrong, J. D. Simple Neurite Tracer: open source software for reconstruction, visualization and analysis of neuronal processes. *Bioinformatics* **27**, 2453–2454 (2011).
56. Kuwajima, M., Mendenhall, J. M. & Harris, K. M. Large-volume reconstruction of brain tissue from high-resolution serial section images acquired by SEM-based scanning transmission electron microscopy. *Methods Mol. Biol.* **950**, 253–273 (2013).
57. Deerinck, T. J., Bushong, E. A., Thor, A. & Ellisman, M. H. NCMIR methods for 3D EM: a new protocol for preparation of biological specimens for serial block face scanning electron microscopy. *Microscopy* **1**, 6–8 (2010).
58. Horstmann, H., Korber, C., Satzler, K., Aydin, D. & Kuner, T. Serial section scanning electron microscopy (S3EM) on silicon wafers for ultra-structural volume imaging of cells and tissues. *PLoS ONE* **7**, e35172 (2012).
59. Hao, Y. et al. Integrated analysis of multimodal single-cell data. *Cell* **184**, 3573–3587 e3529 (2021).

60. Conway, J. R., Lex, A. & Gehlenborg, N. UpSetR: an R package for the visualization of intersecting sets and their properties. *Bioinformatics* **33**, 2938–2940 (2017).
61. Kuleshov, M. V. et al. Enrichr: a comprehensive gene set enrichment analysis web server 2016 update. *Nucleic Acids Res.* **44**, W90–W97 (2016).
62. Liao, Y., Wang, J., Jaehnig, E. J., Shi, Z. & Zhang, B. WebGestalt 2019: gene set analysis toolkit with revamped UIs and APIs. *Nucleic Acids Res.* **47**, W199–W205 (2019).

Acknowledgements

We thank A. Mansour (Salk Institute) for providing the pCSC-CAG-GFP lentiviral labeled H9 ESC line, N. Hah for technical assistance with snRNA-seq and R. Garg for assistance with EM segmentation. We also thank M.L. Gage for editorial comments and A. Cao and T. Bartol for their help with 3DEM visualization. This work was supported by the American Heart Association and the Paul G. Allen Frontiers Group Grant (19PABHI34610000/TEAM LEADER: Fred H. Gage/2019), JPB Foundation, Annette C. Merle-Smith, Lynn and Edward Streim, the Milky Way Foundation, the Ray and Dagmar Dolby Family Fund and NIH (R37 AG072502-03, P30 AG062429-05, P30 AG068635-04, R01 AG070154-04, AG056306-07 and P01 AG051449-08). This work was also supported by the NGS Core Facility, the GT3 Core Facility, the Razavi Newman Integrative Genomics and Bioinformatics Core Facility and the Waitt Advanced Biophotonics Core Facility of the Salk Institute with funding from NIH-NCI (CCSG, P30 014195), the Chapman Foundation, NINDS R24 Core Grant, NEI and the Waitt Foundation. M.W. is supported by a Young Investigator Grant from the Brain & Behavior Research Foundation (BBRPNARSAD) and a Pioneer Fund Postdoctoral Scholar Award from the Salk Institute. Figures 2a, 2h, 4a, 5a, 6a and 6d were created with [BioRender.com](#).

Author contributions

M.W., L.Z. and F.H.G. conceived the study and wrote the paper. M.W., L.Z., C.K.L. and S.F. performed cell culture and organoid differentiation. M.W., L.Z., C.K.L. and I.S.G. performed surgeries. S.L.P. assisted in surgeries. M.W. and I.S.G. performed snRNA-seq and scRNA-seq. M.W., C.Q. and E.M. performed NanoString GeoMx DSP. M.W., M.N.S., J.Y. and A.E.W. performed bioinformatics analyses. M.W. and L.Z. performed imaging analysis with assistance from L.L.X., C.K.L., S.C. and M.D.S. L.Z., S.W.N. and L.R.A. performed sample processing for SEM. S.W.N. and L.R.A. performed electron microscopic image analysis under the supervision of M.W., L.Z. and U.M. F.H.G. provided funding.

Competing interests

The authors declare no competing interests.

Additional information

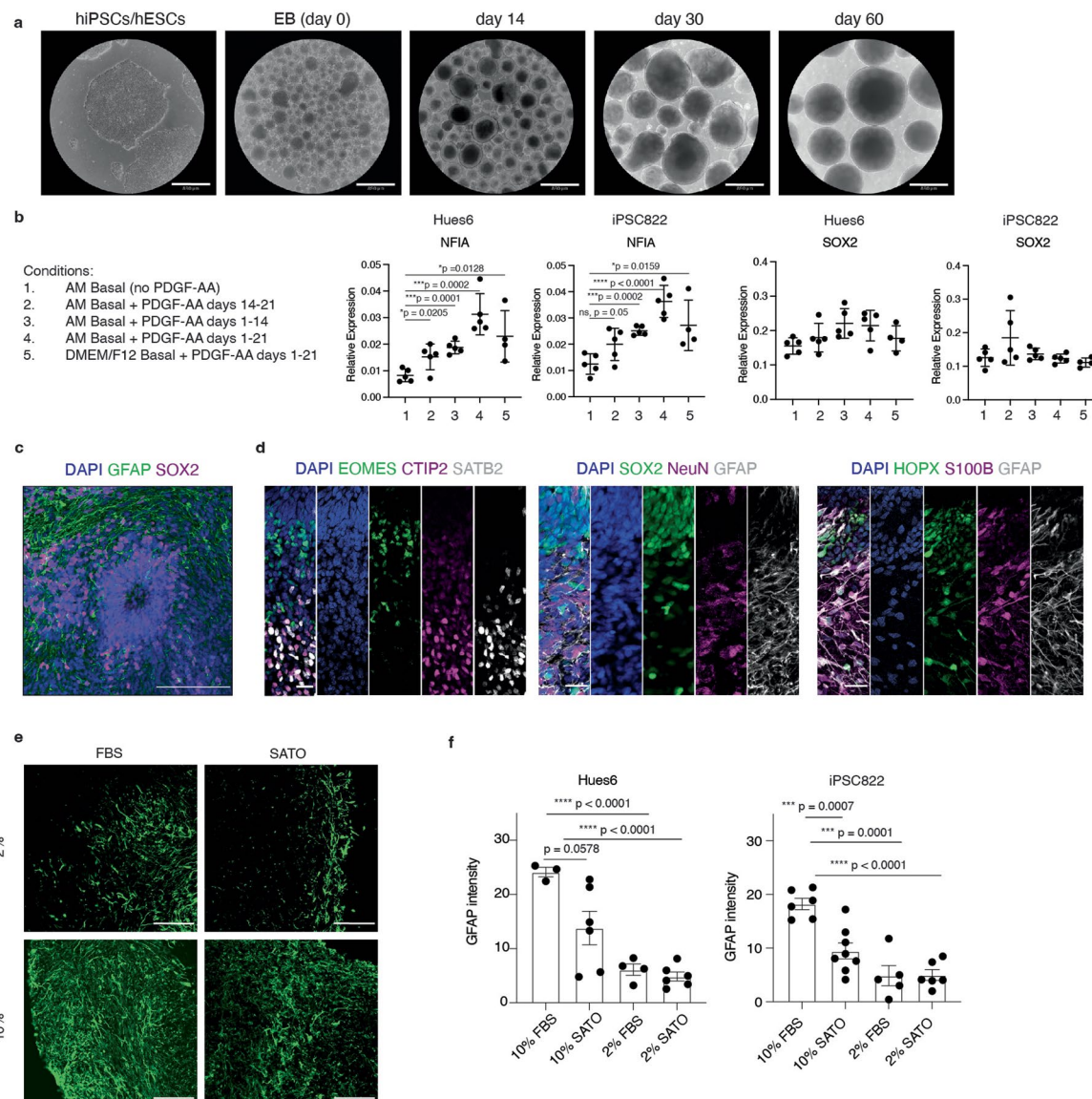
Extended data is available for this paper at <https://doi.org/10.1038/s41587-024-02157-8>.

Supplementary information The online version contains supplementary material available at <https://doi.org/10.1038/s41587-024-02157-8>.

Correspondence and requests for materials should be addressed to Fred H. Gage.

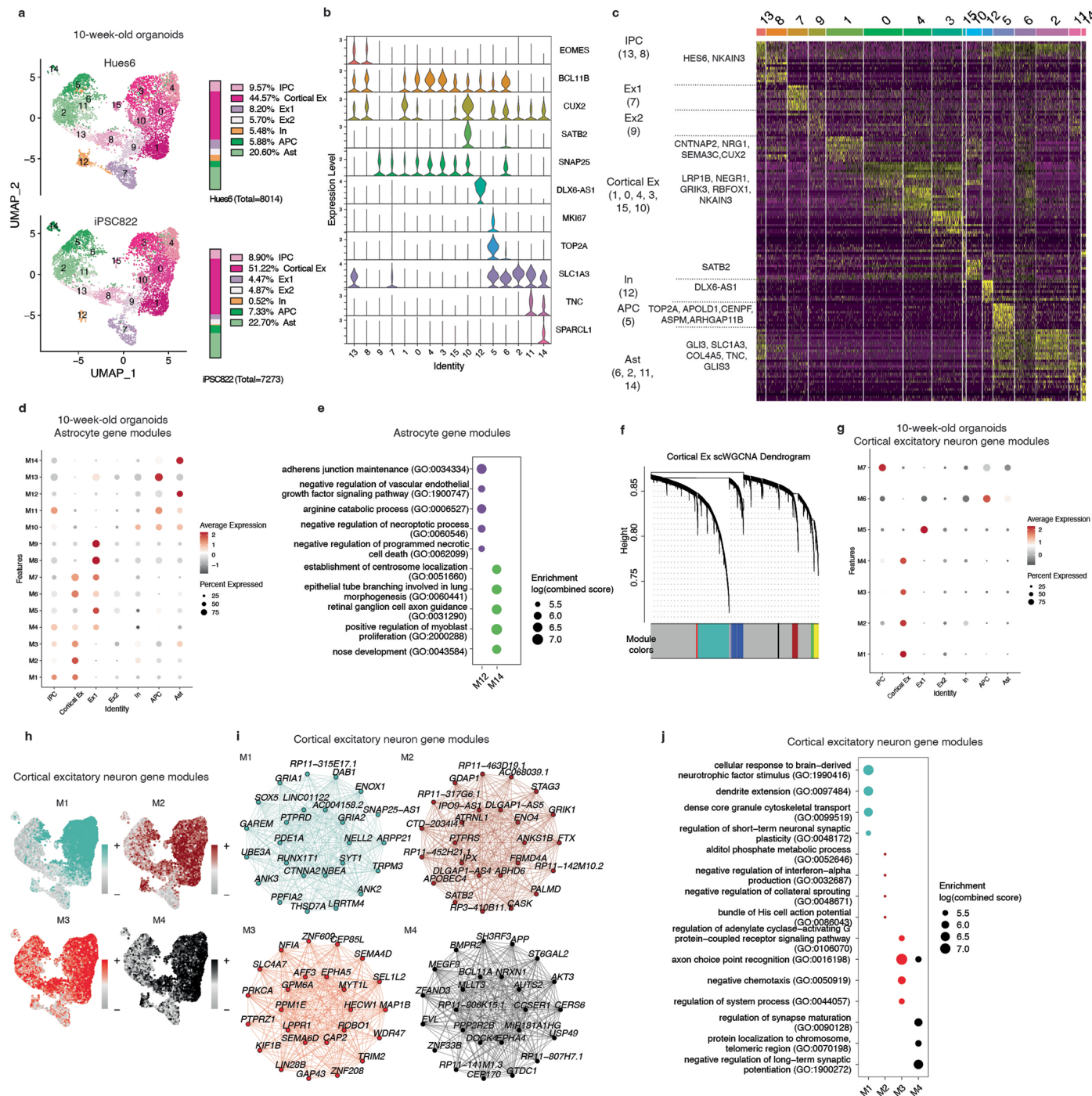
Peer review information *Nature Biotechnology* thanks the anonymous reviewers for their contribution to the peer review of this work.

Reprints and permissions information is available at www.nature.com/reprints.



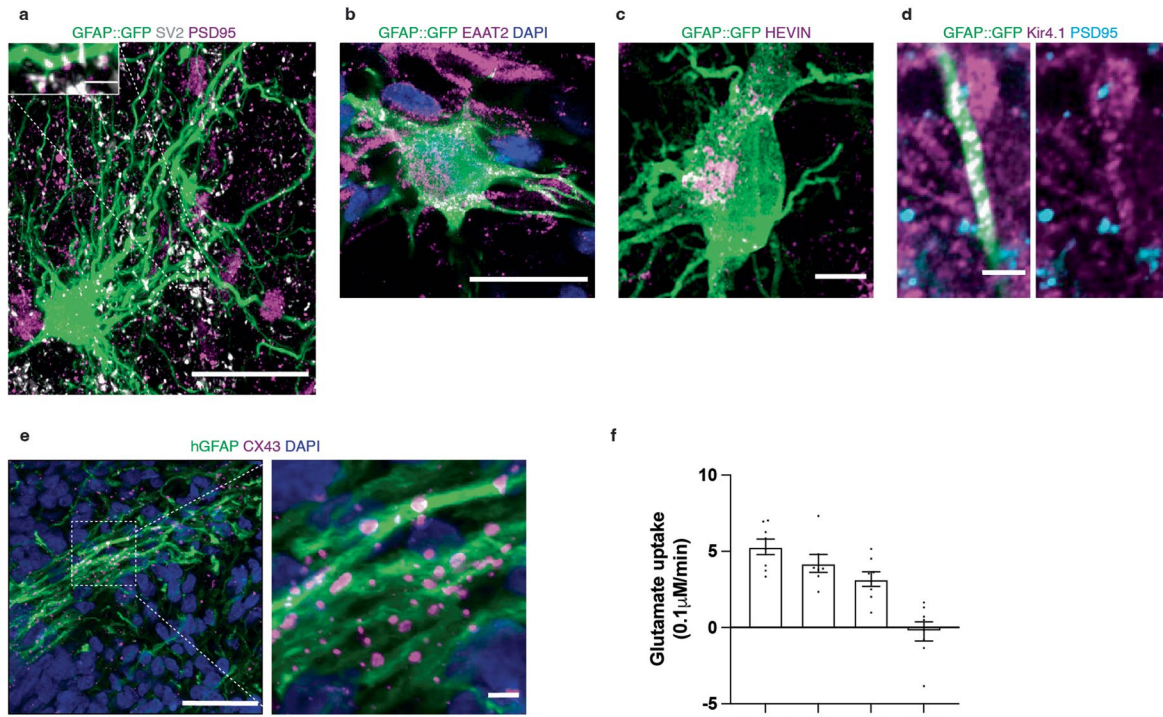
Extended Data Fig. 1 | Rapid astrogliogenesis in glia-enriched cortical organoids. **a.** Sample bright-field images of hiPSCs/hESCs colonies and glia-enriched cortical organoids at days 0, 14, 30 and 60. Day 0 refers to embryoid bodies (EB). Scale bars, 890 μ m. **b.** Quantitative PCR analysis of the expression levels of NFIA and SOX2 in three-week-old organoids cultured under varying conditions (Hues6: 1, n = 5; 2, n = 5; 3, n = 5; 4, n = 5; 5, n = 4. iPSC822: 1, n = 5; 2, n = 5; 3, n = 5; 4, n = 5; 5, n = 4). Each dot represents a pool of three organoids. Bars, mean \pm s.d. Two-sided t-test, ns, not significant, *p < 0.05, **p < 0.001, ***p < 0.0001. **c.** Immunostaining of two-month-old glia-enriched cortical organoids: stem cells (SOX2, magenta), astrocytes (GFAP, green). Scale bar, 100 μ m. **d.** Immunostaining of two-month-old glia-enriched cortical organoids: intermediate progenitor cells (EOMES, green), cortical excitatory neurons

(CTIP2, magenta; SATB2, gray), stem cells (SOX2, green), neurons (NeuN, magenta), astrocytes (GFAP, gray), glia (HOPX, green; S100B, magenta; GFAP, gray). Scale bars, 20 μ m. **e.** Immunostaining of three-month-old glia-enriched cortical organoids differentiated in 2% FBS (top left panel), 2% SATO (top right panel); serum-free condition, SATO component reported in ref. 30), 10% FBS (bottom left panel) and 10% SATO (bottom right panel). Astrocytes (GFAP, green). Scale bars, 100 μ m. **f.** Quantification of the GFAP fluorescence intensity in glia-enriched cortical organoids differentiated in 2% FBS, 2% SATO, 10% FBS and 10% SATO conditions (Hues6: 10% FBS, n = 3; 10% SATO, n = 6; 2% FBS, n = 4; 2% SATO, n = 6. iPSC822: 10% FBS, n = 6; 10% SATO, n = 8; 2% FBS, n = 5; 2% SATO, n = 6). Each dot represents one organoid. Bars, mean \pm s.e.m. Two-sided t-test, ***p < 0.001, ****p < 0.0001.



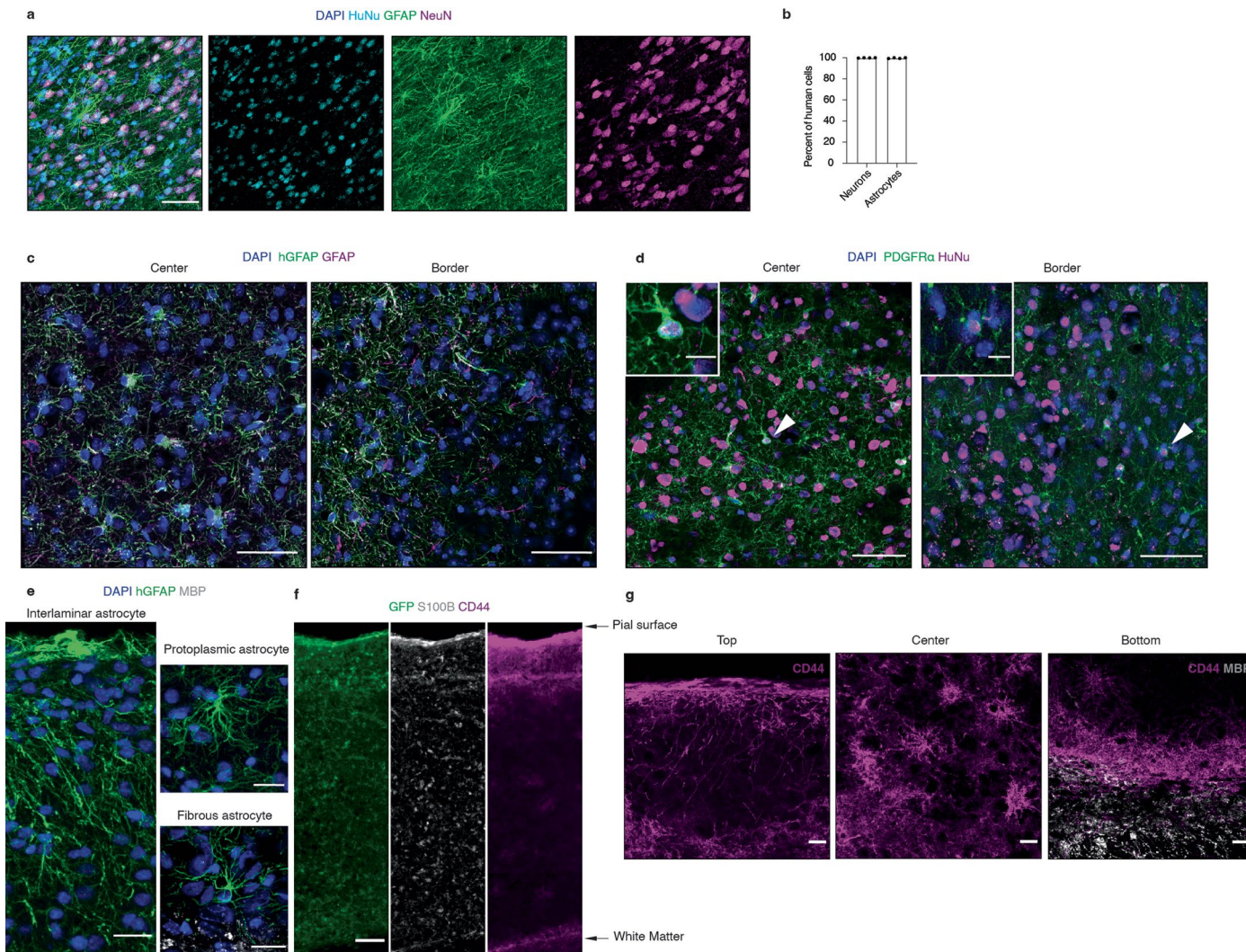
Extended Data Fig. 2 | snRNA-seq of 10-week-old glia-enriched cortical organoids. **a.** UMAP plot of snRNA-seq data from 10-week-old glia-enriched cortical organoids. The percentage of each major cell types is shown. APC, astrocyte progenitor cell; Ast, astrocyte; IPC, intermediate progenitor cell; In, inhibitory neuron; Cortical Ex, cortical excitatory neuron; Ex1 and Ex2, excitatory neuron. **b.** Expression of selected marker genes used in cell type identification. The violin plot shows the distribution of normalized expression in nuclei in each cluster. Scale: normalized read counts. **c.** Heatmap plot shows the expression of the top 10 feature genes identified in each cluster. **d.** Dot plot shows the

expression of astrocyte gene modules in each major cell type. **e.** Dot plot of the enrichR combined score for the top enriched GO terms for astrocyte gene modules M12 and M14. **f.** WGCNA dendrogram of Cortical Ex gene modules. **g.** Dot plot shows the expression of Cortical Ex gene modules in each major cell type. **h.** UMAP plots of module hub gene expression score for Cortical Ex gene modules M1–4. **i.** Co-expression plots of the top 25 module genes for Cortical Ex gene modules M1–4. **j.** Dot plot of the enrichR combined score for the top enriched GO terms for cortical excitatory neuron gene modules M1–4.



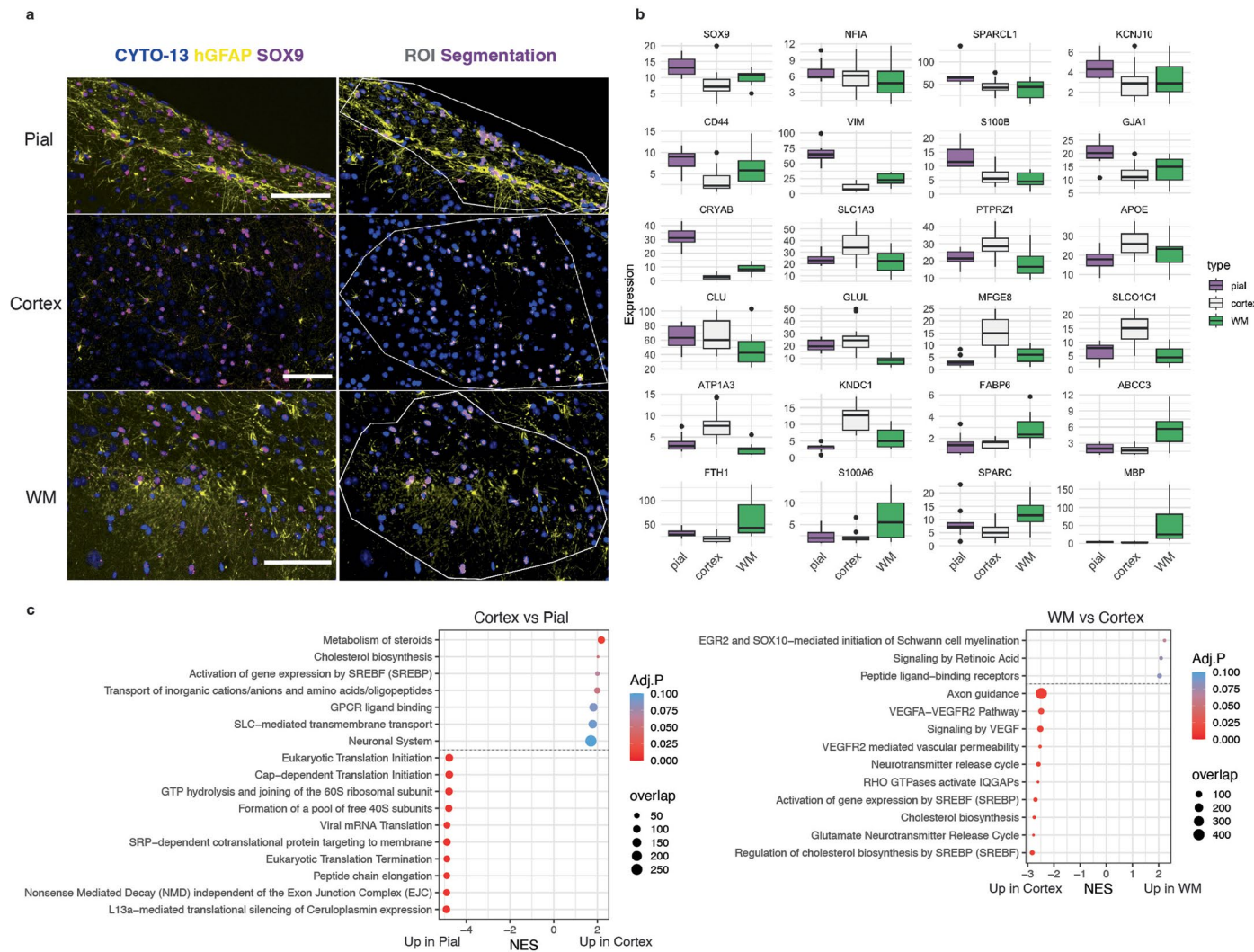
Extended Data Fig. 3 | Maturation of astrocytes in glia-enriched cortical organoids. **a.** Immunostaining of five-month-old glia-enriched cortical organoids: GFAP::GFP AAV-labeled astrocytes (GFP, green), presynaptic vesicles (SV2, gray), postsynaptic density (PSD95, magenta). Inset, an enlarged view of astrocyte process and synapses. Scale bars, 20 μ m and 2 μ m (inset). **b.** Immunostaining of five-month-old glia-enriched cortical organoids: GFAP::GFP AAV-labeled astrocytes (GFP, green), glutamate transporter (EAAT2, magenta). Scale bar, 20 μ m. **c.** Immunostaining of five-month-old glia-enriched cortical organoids: GFAP::GFP AAV-labeled astrocytes (GFP, green) and matricellular protein (HEVIN, magenta). Scale bar, 5 μ m. **d.** Immunostaining

of five-month-old glia-enriched cortical organoids: GFAP::GFP AAV-labeled astrocytes (GFP, green), inward-rectifier potassium channel (Kir4.1, magenta), postsynaptic density protein (PSD95, cyan). Scale bar, 2 μ m. **e.** Immunostaining of five-month-old glia-enriched cortical organoids: astrocytes (hGFAP, green), Connexin 43 (CX43, magenta). Inset, an enlarged view of astrocyte processes and expression of Connexin 43. Scale bars, 20 μ m and 2 μ m (inset). **f.** Quantification of glutamate uptake of neural progenitor cells (NPCs, n = 8) and astrocytes purified from five-month-old glia-enriched cortical organoids derived from Hues6 (n = 8), iPSC822 (n = 8) and H9 (n = 7) stem cell lines. Each dot represents one independent experiment. Bars, mean \pm s.e.m.



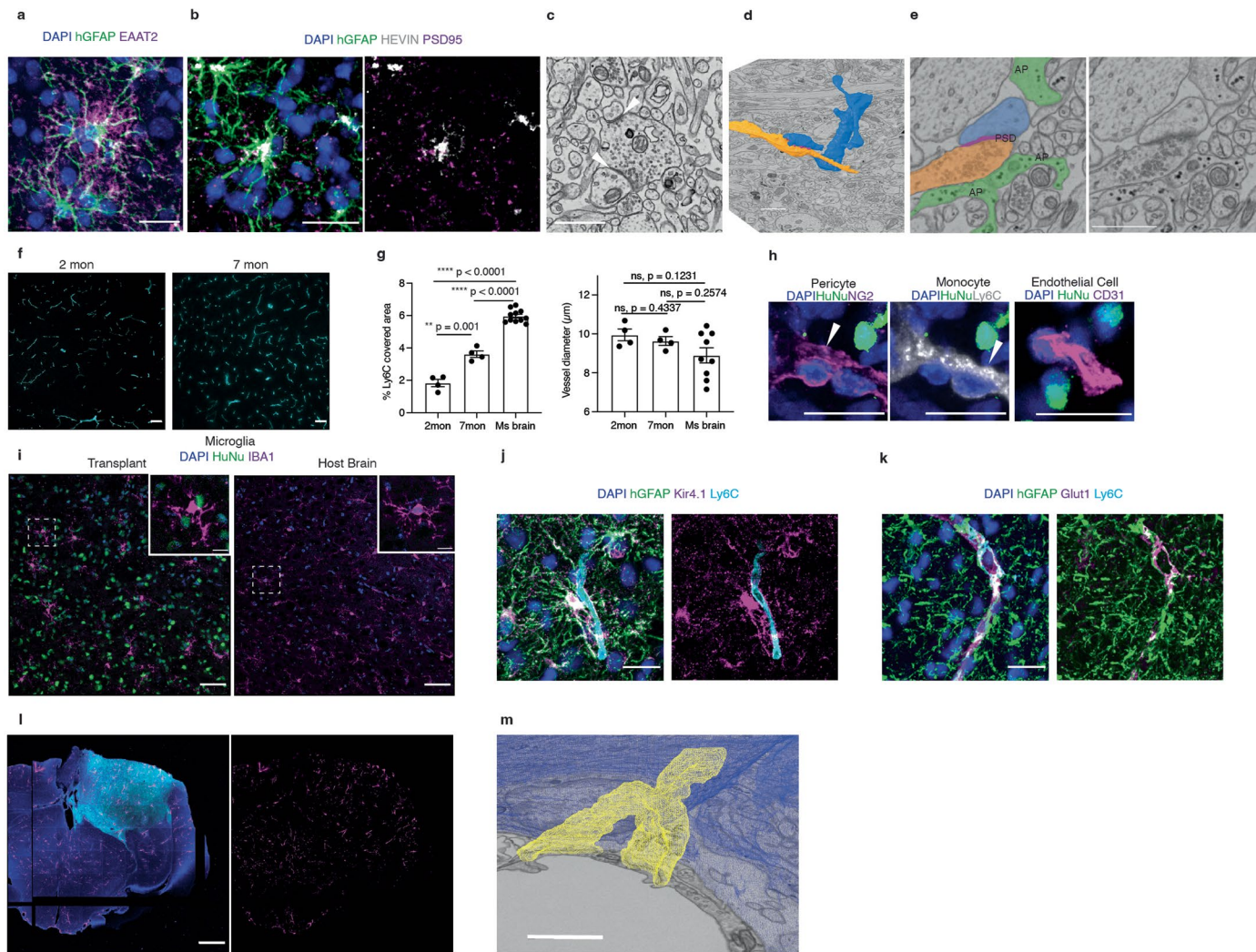
Extended Data Fig. 4 | Formation of anatomically defined morphological subclasses of human astrocytes in engrafted glia-enriched cortical organoids. **a.** Immunostaining of glia-enriched cortical organoid transplants: human nuclear antigen (HuNu, Cyan), astrocytes (GFAP, green), neurons (NeuN, magenta). Scale bar, 20 μ m. **b.** Quantification of the percentage of NeuN $^+$ HuNu $^+$ cells among NeuN $^+$ cells (left) or huGFAP $^+$ GFAP $^+$ cells among GFAP $^+$ cells (right) in the transplants. $n = 4$ transplants. Bars, mean \pm s.e.m. **c.** Immunostaining of the center (left) and border (right) of glia-enriched cortical organoid transplants: human astrocytes (hGFAP, green), astrocytes (GFAP, magenta). Scale bars, 50 μ m. **d.** Immunostaining of the center (left) and border (right) of glia-enriched cortical organoid transplants: oligodendrocyte progenitor cells

(PDGFR α , green), human nuclear antigen (HuNu, magenta). Inset, enlarged views of human oligodendrocyte progenitor cells. Scale bars, 50 μ m and 10 μ m (inset). **e.** Immunostaining of human interlaminar, protoplasmic and fibrous astrocytes in glia-enriched cortical organoid transplants: human astrocytes (hGFAP, green), white matter (myelin basic protein or MBP, gray). Scale bars, 20 μ m. **f.** Immunostaining of glia-enriched cortical organoid transplants: human cells (GFP, green), astrocytes (S100B, gray; CD44, magenta). Scale bar, 100 μ m. **g.** Immunostaining of the top, center and bottom regions of the transplants: astrocytes (CD44, magenta), white matter (myelin basic protein or MBP, gray). Scale bars, 20 μ m.



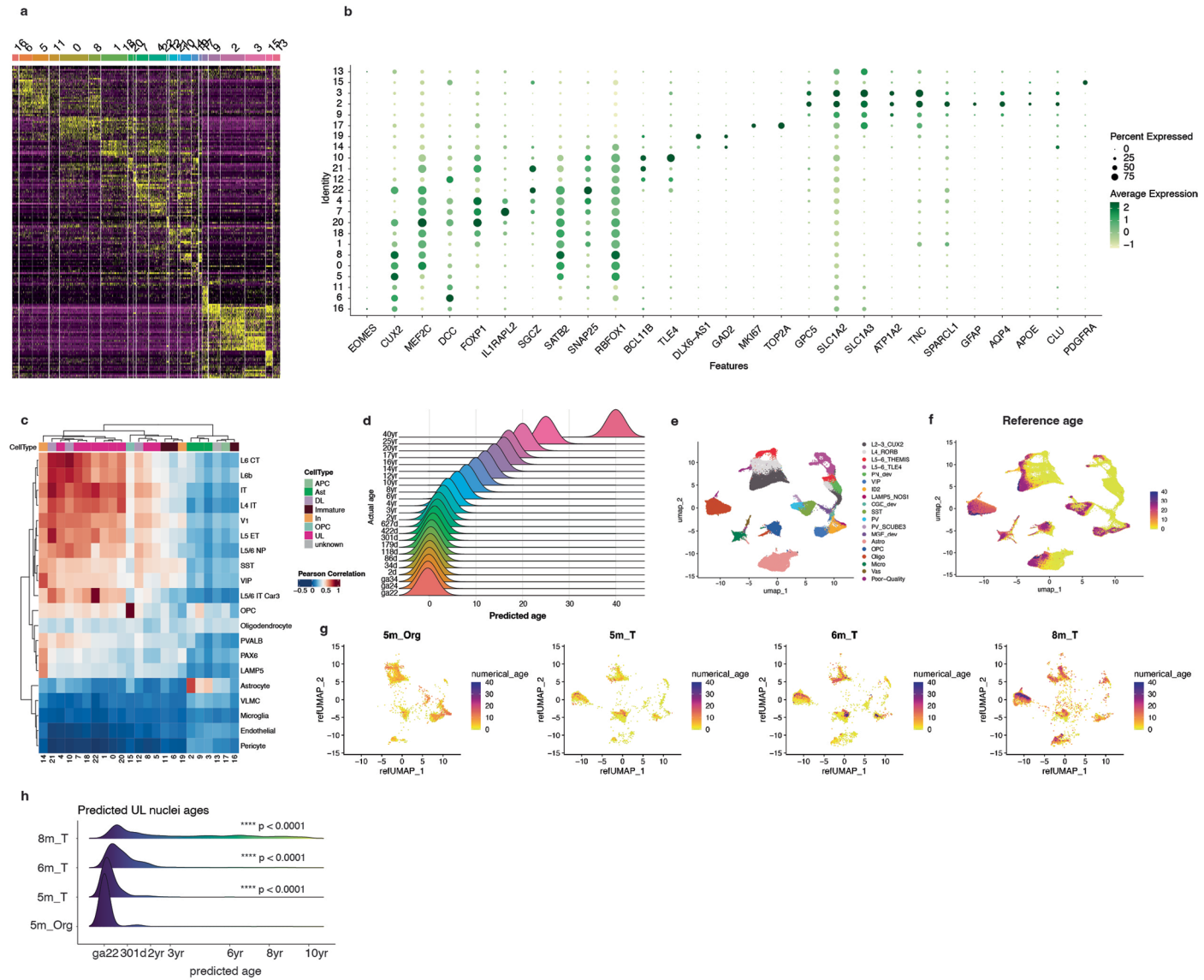
Extended Data Fig. 5 | Spatial transcriptome profiling of layer-specific subclasses of human astrocytes in engrafted glia-enriched cortical organoids. **a.** Immunofluorescent staining images on the left showing hGFAP in yellow, SOX9 in magenta and CYTO-13 in blue, along with the cell segmentation of SOX9⁺/CYTO-13⁺ cells depicted in magenta within a selected ROI on the right. Scale bars, 100 μ m. **b.** Box plots depicting the normalized expression levels

of selected genes in each group (pial = 10 ROIs, cortex = 16 ROIs, WM = 12 ROIs). Centerline, median; box limits, upper and lower quartiles; whiskers, 1.5 \times interquartile range; points, outliers. **c.** Bubble plots depicting top significant terms identified from GSEA using a weighted Kolmogorov-Smirnov test. NES, normalized enrichment score. Significant thresholds set at adjusted p value < 0.1 .



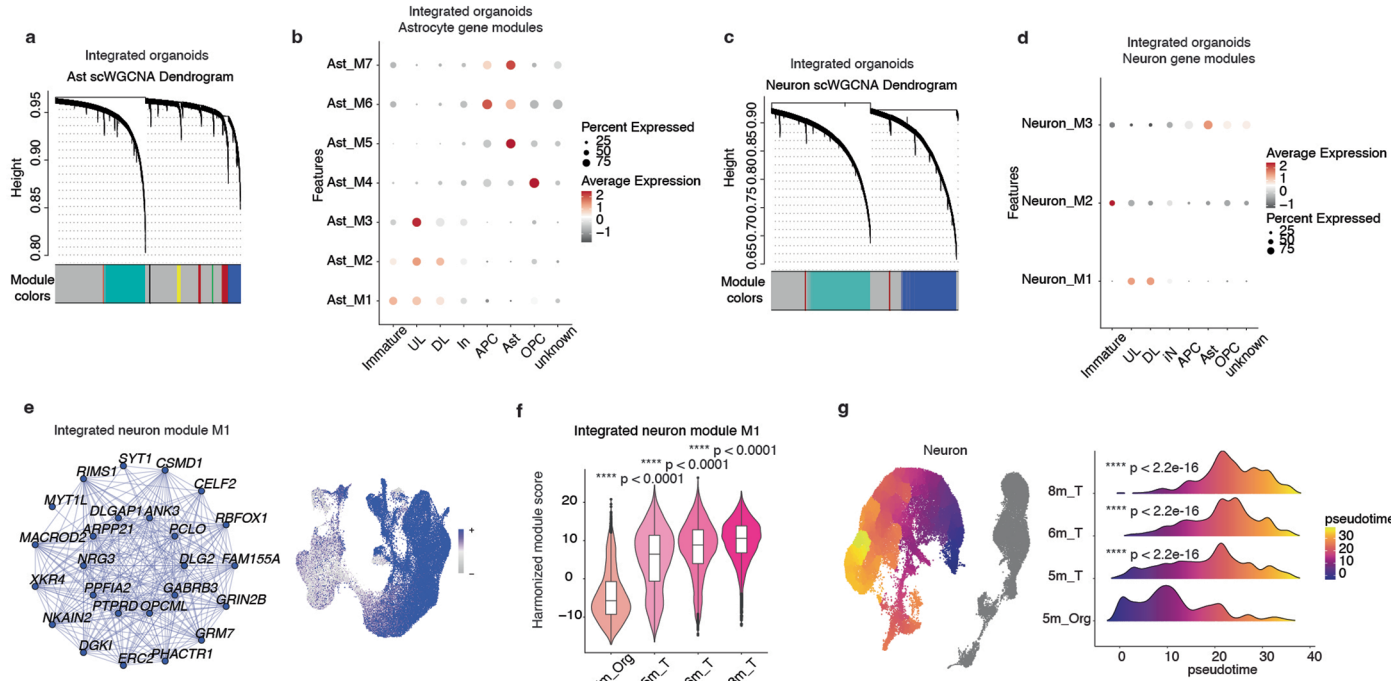
Extended Data Fig. 6 | Close association of human protoplasmic astrocytes with synapses and host vasculature in engrafted glia-enriched cortical organoids. **a**, Immunostaining of transplants: human astrocytes (hGFAP, green), glutamate transporters (EAAT2, magenta). Scale bar, 20 µm. **b**, Immunostaining of transplants: human astrocytes (hGFAP, green), matricellular protein (HEVIN, gray), postsynaptic density (PSD95, magenta). Scale bar, 20 µm. **c**, Electron micrograph of a multi-synaptic bouton in an eight-month-old transplant. Arrowheads: synapses. Scale bar, 1 µm. **d**, 3D reconstruction of serial section electron microscope images of synaptic structures in an eight-month-old transplant. Presynaptic bouton (orange), postsynaptic density (magenta), dendritic spine (blue). Scale bar, 1 µm. **e**, Electron micrograph of a synapse within the transplant. Left, presynaptic bouton (orange), postsynaptic density (PSD, magenta), dendritic spine (blue) and astrocytic processes (AP, green). Right, original image. Scale bar, 1 µm. **f**, Immunostaining of transplants at 2 (left panel) or 7 months (right panel) post-transplantation: blood vessels (Ly6C, cyan). Scale bars, 100 µm. **g**, Ly6C⁺ area (left) or vessel diameter (right) in transplants at 2 months (n = 4 transplants) or 7 months (n = 4 transplants) post-transplantation versus contralateral mouse cortex (Ms brain; n = 8 mice). Bars, mean ± s.e.m. Two-sided t-test, **p = 0.001, ****p < 0.0001. **h**, Immunostaining of transplants: human nuclear antigen (HuNu, green), pericytes (NG2, magenta, indicated by arrowhead in the left image), monocytes (Ly6C, gray, indicated by arrowhead in the middle image), endothelial cells (CD31, magenta). Scale bars, 10 µm. **i**, Immunostaining of transplants (left) or host brains (right): human nuclear antigen (HuNu, green), microglia (IBA1, magenta). Inset: microglia. Scale bars, 50 µm and 10 µm (insets). **j**, Immunostaining of transplants: human astrocytes (hGFAP, green), inward-rectifier potassium channel (Kir4.1, magenta), blood vessels (Ly6C, cyan). Scale bar, 20 µm. **k**, Immunostaining of transplants: human astrocytes (hGFAP, green), glucose transporter (Glut1, magenta) and blood vessels (Ly6C, cyan). Scale bar, 20 µm. **l**, Confocal images of the transplant used in EM studies: blood vessels (Dil, magenta), transplant (GFP, green). Scale bar, 1 mm. **m**, 3D reconstruction of series SEM images: tight junction (yellow) and basement membrane (blue). Scale bar, 1 µm.

2 months (n = 4 transplants) or 7 months (n = 4 transplants) post-transplantation versus contralateral mouse cortex (Ms brain; n = 8 mice). Bars, mean ± s.e.m. Two-sided t-test, **p = 0.001, ****p < 0.0001. **h**, Immunostaining of transplants: human nuclear antigen (HuNu, green), pericytes (NG2, magenta, indicated by arrowhead in the left image), monocytes (Ly6C, gray, indicated by arrowhead in the middle image), endothelial cells (CD31, magenta). Scale bars, 10 µm. **i**, Immunostaining of transplants (left) or host brains (right): human nuclear antigen (HuNu, green), microglia (IBA1, magenta). Inset: microglia. Scale bars, 50 µm and 10 µm (insets). **j**, Immunostaining of transplants: human astrocytes (hGFAP, green), inward-rectifier potassium channel (Kir4.1, magenta), blood vessels (Ly6C, cyan). Scale bar, 20 µm. **k**, Immunostaining of transplants: human astrocytes (hGFAP, green), glucose transporter (Glut1, magenta) and blood vessels (Ly6C, cyan). Scale bar, 20 µm. **l**, Confocal images of the transplant used in EM studies: blood vessels (Dil, magenta), transplant (GFP, green). Scale bar, 1 mm. **m**, 3D reconstruction of series SEM images: tight junction (yellow) and basement membrane (blue). Scale bar, 1 µm.



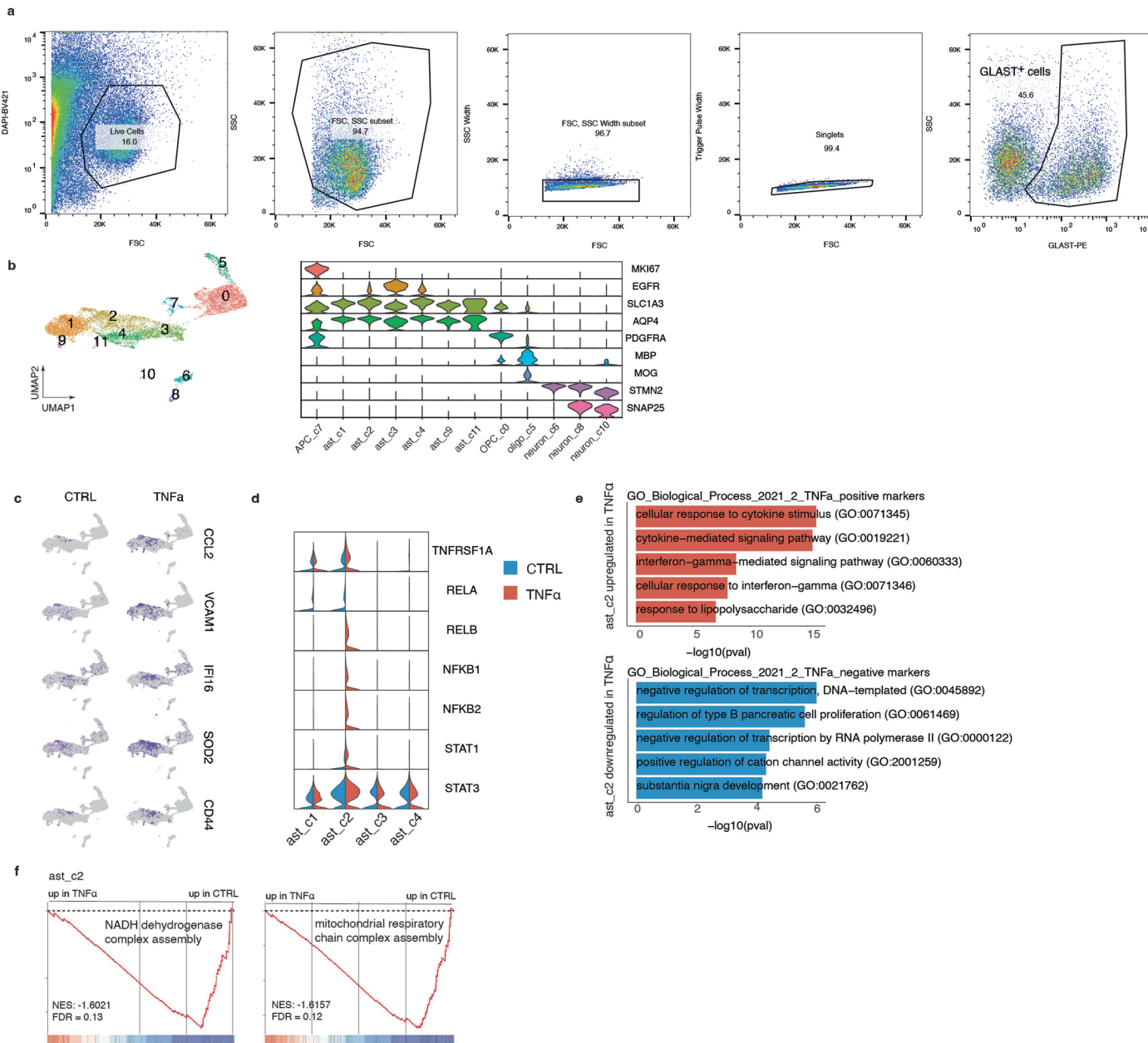
Extended Data Fig. 7 | Transcriptomic analysis of integrated snRNA-seq datasets. **a.** Heatmap plot shows the expression levels of the top 10 feature genes identified in each cluster. **b.** Dot plot shows the average expression of selected marker genes in nuclei in each cluster. **c.** Heatmap depicting the pairwise transcriptional cluster correlation of cell clusters using top 50 marker genes from each cluster in integrated organoid datasets with cell clusters in snRNA-seq datasets of multiple human cortical areas from Allen Brain Map. Immature, immature excitatory neuron; UL, upper layer cortical excitatory neuron; DL, deep-layer cortical excitatory neuron; In, inhibitory neuron; APC, astrocyte progenitor cell; Ast, astrocyte; OPC, oligodendrocyte progenitor cell; unknown, undetermined cell. **d.** Ridge plot shows the distributions of predicted age for

nuclei derived from snRNA-seq data obtained from prefrontal cortex (PFC) samples ranging from 22 weeks of gestation (ga) to 40 years of age (ref. 34). **e.** t-SNE plot of snRNA-seq data from PFC samples (ref. 34) colored by major cell types. **f.** t-SNE plot of snRNA-seq data from PFC samples (ref. 34) with each nucleus colored by its donor age. **g.** t-SNE plots of snRNA-seq data from 5-month-old organoids (5m_Org), 5-month-old transplants (5m_T), 6-month-old transplants (6m_T) and 8-month-old transplants (8m_T), projected on to the reference dataset, with each nucleus colored by the predicted age. **h.** Ridge plot shows the distributions of predicted age for UL nuclei from 5m_Org, 5m_T, 6m_T and 8m_T. Wilcoxon test (two-sided, ****, p < 0.0001; reference group, 5m_Org).



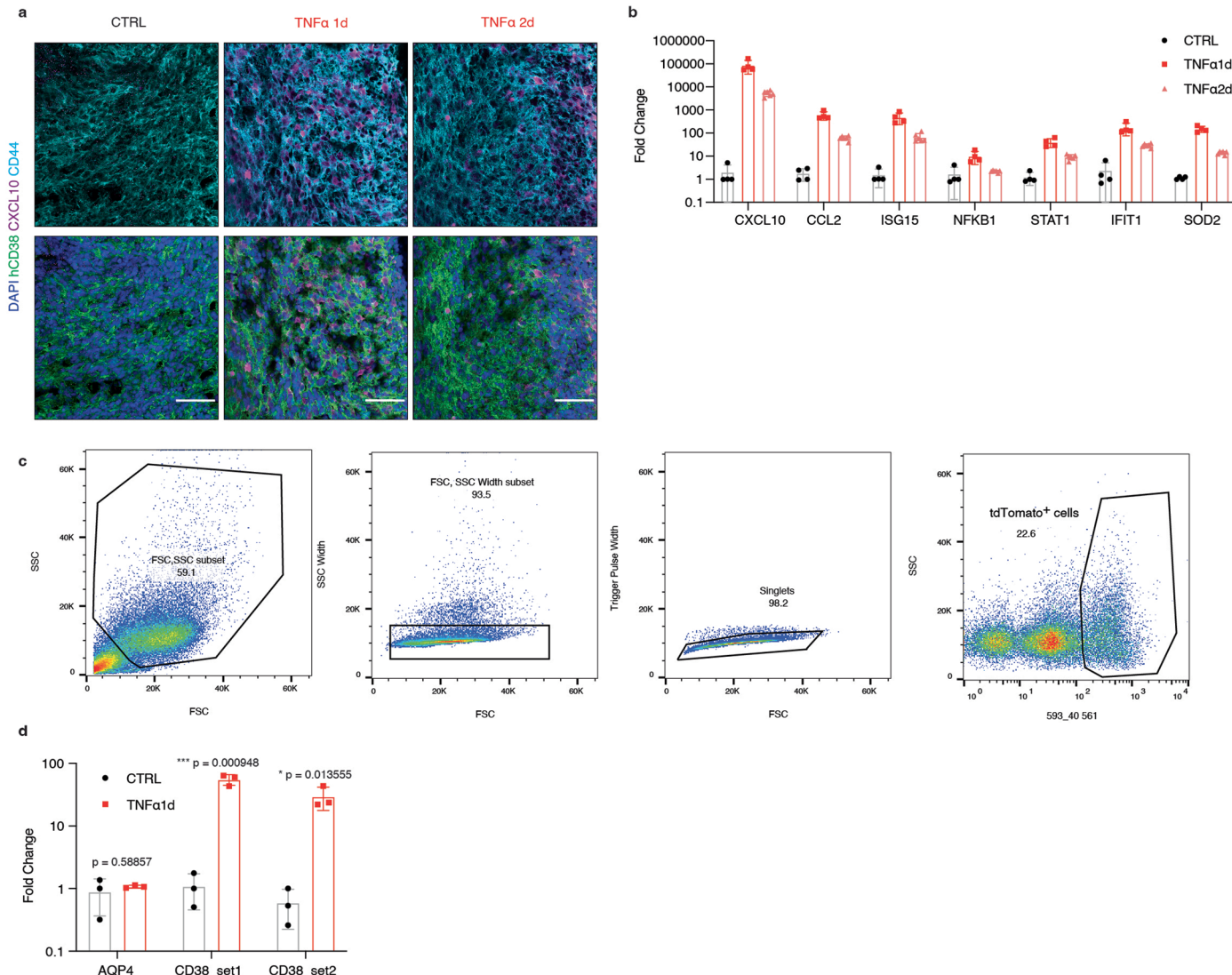
Extended Data Fig. 8 | WGCNA and pseudotime analyses of integrated snRNA-seq datasets. **a.** WGCNA dendrogram of gene modules constructed from astrocytes across different time points. **b.** Dot plot shows the expression levels of astrocyte gene modules across major cell type. **c.** WGCNA dendrogram of gene modules constructed from immature and UL excitatory neurons across different time points. **d.** Dot plot shows the expression levels of neuron gene modules in each major cell type. **e.** Co-expression plot of the top 25 hub genes (left) and UMAP plot (right) of module hub gene expression score for neuron gene

modules M1. **f.** Violin plot of harmonized module score of neuron gene module M1 in UL excitatory neurons across different time points. Centerline, median; box limits, upper and lower quartiles; whiskers, 1.5× interquartile range; points, outliers. Wilcoxon test (two-sided, ****, p < 0.0001; reference group, 5m_Org). **g.** UMAP dimensionality reduction displays the pseudotime trajectories of neurons from the integrated snRNA-seq. Each cell is colored by its pseudotime trajectory assignment. Pseudotime analysis separated by time point. One-sided Kolmogorov–Smirnov test (****, p < 2.2e-16; reference group, 5m_Org).



Extended Data Fig. 9 | Transcriptome profiling reveals rapid activation of pro-inflammatory pathways in a subpopulation of astrocytes in vivo.
a. Flow cytometry sorting strategy for glial cells. **b.** UMAP plot (left) and violin plot (right) shows the expression of selected cell type marker genes. **c.** UMAP plots show the expression of selected genes. **d.** Violin plot shows the expression of selected genes in astrocyte clusters 1–4. Ast, astrocyte. **e.** Bar plot of the

enrichR combined score for gene ontology terms of the top 100 significantly upregulated (top) and downregulated (bottom) genes following TNF α treatment in cluster 2 astrocytes. **f.** GSEA comparing TNF α -treated and saline-treated cluster 2 astrocytes. GO terms are shown. FDR, false discovery rate; NES, normalized enrichment score.



Extended Data Fig. 10 | CD38 mediates inflammation-induced metabolic and mitochondrial stresses in human astrocytes. **a.** Immunostaining of in vitro glia-enriched cortical organoids at day 0, day 1 and day 2 post-TNF α treatment: astrocytes (hCD38, green; CD44 cyan), chemokines (CXCL10, magenta). Scale bars, 50 μ m. **b.** Quantitative PCR analyses of selected genes in organoids (CTRL = 4; TNF α 1d = 4; TNF α 2d = 6). Each dot represents one organoid. Bars,

mean \pm s.d. **c.** Flow cytometry sorting strategy for GFAP::tdTomato $^{+}$ cells.

d. Quantitative PCR analyses of selected genes in sorted astrocytes (CTRL = 3 independent experiments; TNF α 1d = 3 independent experiments). Each dot represents one independent experiment. Bars, mean \pm s.d. Two-sided t-test, *p = 0.013555, ***p = 0.000948.

Fred Gage

Corresponding author(s): _____

Last updated by author(s): Jan 24, 2024

Reporting Summary

Nature Portfolio wishes to improve the reproducibility of the work that we publish. This form provides structure for consistency and transparency in reporting. For further information on Nature Portfolio policies, see our [Editorial Policies](#) and the [Editorial Policy Checklist](#).

Statistics

For all statistical analyses, confirm that the following items are present in the figure legend, table legend, main text, or Methods section.

n/a Confirmed

- The exact sample size (n) for each experimental group/condition, given as a discrete number and unit of measurement
- A statement on whether measurements were taken from distinct samples or whether the same sample was measured repeatedly
- The statistical test(s) used AND whether they are one- or two-sided
Only common tests should be described solely by name; describe more complex techniques in the Methods section.
- A description of all covariates tested
- A description of any assumptions or corrections, such as tests of normality and adjustment for multiple comparisons
- A full description of the statistical parameters including central tendency (e.g. means) or other basic estimates (e.g. regression coefficient) AND variation (e.g. standard deviation) or associated estimates of uncertainty (e.g. confidence intervals)
- For null hypothesis testing, the test statistic (e.g. F , t , r) with confidence intervals, effect sizes, degrees of freedom and P value noted
Give P values as exact values whenever suitable.
- For Bayesian analysis, information on the choice of priors and Markov chain Monte Carlo settings
- For hierarchical and complex designs, identification of the appropriate level for tests and full reporting of outcomes
- Estimates of effect sizes (e.g. Cohen's d , Pearson's r), indicating how they were calculated

Our web collection on [statistics for biologists](#) contains articles on many of the points above.

Software and code

Policy information about [availability of computer code](#)

Data collection SmartSEM (Zeiss) and Atlas5 (Fibics) were used for control software in scanning electron microscopy. Zen (Zeiss) software was used for acquiring immunohistochemistry images. GeoMx Digital Spatial Profiler (NanoString) was used for acquiring spatial genomics.

Data analysis MATLAB(2021b, 2022b), Fiji ImageJ (v2.3.0/1.53f, NIH), GraphPad Prism (v9.3.1, GraphPad), Zen (Zeiss), VAST Lite, Blender, Neuromorph, GAMer, SimpleNeuriteTracer v3.1.7, CellRanger (v6.0.1, 10x Genomics), R (v4.1.2), Seurat (v4.1.0, v4.2.0), Monocle 3(v1.0.0), scWGCNA (v0.0.0.9000), UpSetR (v1.4.0), FNN R package (v1.1.3), WebGestalt R package (v0.4.4), GeoMx DSP Data Analysis Suite (v3.0.0.182), Handbrake (v1.6.1)

For manuscripts utilizing custom algorithms or software that are central to the research but not yet described in published literature, software must be made available to editors and reviewers. We strongly encourage code deposition in a community repository (e.g. GitHub). See the Nature Portfolio [guidelines for submitting code & software](#) for further information.

Data

Policy information about [availability of data](#)

All manuscripts must include a [data availability statement](#). This statement should provide the following information, where applicable:

- Accession codes, unique identifiers, or web links for publicly available datasets
- A description of any restrictions on data availability
- For clinical datasets or third party data, please ensure that the statement adheres to our [policy](#)

Single nucleus RNA-seq data is available in GEO under the accession number GSE185472. The following public datasets were used for snRNA-seq analysis: Allen Brain Institute human adult snRNA-seq data from multiple cortical areas (<https://portal.brain-map.org/atlas-and-data/rnaseq/human-multiple-cortical-areas-smart-seq>; accessed October 2022), snRNA-seq data from broad temporal coverage from fetal to adulthood stages of the Brodmann area 8, 9, 10, and 46 prefrontal cortex regions (Gene Expression Omnibus accession number GSE168408), and snRNA-seq from eight-month-old cortical organoid transplants (Gene Expression Omnibus accession number GSE190815). For single-nucleus analysis, we used hg19 human reference genome v1.2.0 and mm10 mouse reference genome v1.2.0 provided by 10X. The sequences and gene files used to build the references can be achieved at ftp://ftp.ensembl.org/pub/grch37/release-84/fasta/homo_sapiens/dna/ and ftp://ftp.ensembl.org/pub/grch37/release-84/gtf/homo_sapiens/ (for human hg19 genome); ftp://ftp.ensembl.org/pub/release-84/fasta/mus_musculus/dna/ and ftp://ftp.ensembl.org/pub/release-84/gtf/mus_musculus/ (for mouse mm10 genome). All other raw data used for plotting in the figures are provided as Source Data.

Human research participants

Policy information about [studies involving human research participants](#) and [Sex and Gender in Research](#).

Reporting on sex and gender	Not applicable
Population characteristics	Not applicable
Recruitment	Not applicable
Ethics oversight	Not applicable

Note that full information on the approval of the study protocol must also be provided in the manuscript.

Field-specific reporting

Please select the one below that is the best fit for your research. If you are not sure, read the appropriate sections before making your selection.

Life sciences Behavioural & social sciences Ecological, evolutionary & environmental sciences

For a reference copy of the document with all sections, see nature.com/documents/nr-reporting-summary-flat.pdf

Life sciences study design

All studies must disclose on these points even when the disclosure is negative.

Sample size	Sample size for each experiment was indicated in the figure legends for each experiment. The sample size was chosen based on previous experience for each experiment. No statistical tests were used to predetermine sample size.
Data exclusions	For snRNA-seq and scRNA_seq analysis, mouse nuclei and low quality nuclei were removed from the analysis. A detailed description of single nucleus and single cell exclusions can be found in the Methods section.
Replication	The data presented from representative experiments were independently replicated at least three times with similar outcomes, unless explicitly indicated by the sample size noted in each figure or Method section. This includes all microscopy data and quantitative PCR data.
Randomization	Organoids or transplants were randomly allocated into different groups to ensure unbiased distribution of variables and comparability across treatments.
Blinding	In this study, blinding of the investigators was not implemented due to the distinct and apparent differences between in vivo and in vitro organoid models, as well as the evident differences observed in organoids at various developmental stages.

Reporting for specific materials, systems and methods

We require information from authors about some types of materials, experimental systems and methods used in many studies. Here, indicate whether each material, system or method listed is relevant to your study. If you are not sure if a list item applies to your research, read the appropriate section before selecting a response.

Materials & experimental systems

n/a	<input type="checkbox"/> Involved in the study <input checked="" type="checkbox"/> Antibodies <input type="checkbox"/> Eukaryotic cell lines <input checked="" type="checkbox"/> Palaeontology and archaeology <input type="checkbox"/> Animals and other organisms <input checked="" type="checkbox"/> Clinical data <input checked="" type="checkbox"/> Dual use research of concern
-----	--

Methods

n/a	<input type="checkbox"/> Involved in the study <input checked="" type="checkbox"/> ChIP-seq <input checked="" type="checkbox"/> Flow cytometry <input checked="" type="checkbox"/> MRI-based neuroimaging
-----	--

Antibodies

Antibodies used

Primary antibodies:

anti-NFIA (rabbit, ab41851, Abcam; 1:250), anti-SOX2 (rat, 14-9811-82, clone#Btjce, Invitrogen; 1:400), anti-GFAP (rabbit, Z0334, Dako; 1:500), anti-GFAP (chicken, AB5541, EMD Millipore; 1:1000), anti-GFP (chicken, GFP-1020, Aves lab; 1:1000), anti-hGFAP (mouse, Y40420, clone# not provided by vendor, TaKaRa; 1:500), anti-Human Nuclear Antigen (HuNu) (mouse, ab215755, clone#235-1, Abcam; 1:250), anti-NeuN (rabbit, ABN78, EMD Millipore; 1:250), anti-Ly6C (rat, ab15627, Clone# ER-MP20, Abcam; 1:500), anti-Aquaporin 4 (AQP4) (rabbit, AQP-004, Alomone Labs; 1:400), anti-Kir4.1 (rabbit, APC-035, Alomone Labs; 1:250), anti-glucose transporter GLUT1 (rabbit, ab115730, Abcam; 1:100), anti-tdTomato (rabbit, 600-401-379, Rockland; 1:500), anti-Laminin (rabbit, NB300-144SS, Novus a biotchnie brand; 1:500), anti-hHepaCAM (mouse, MAB4108, clone#419305, R&D Systems; 1:400), anti-S100B (rabbit, ab52642, Abcam; 1:1000), anti-TBR2/Eomes (rabbit, ab275960, Abcam; 1:250), anti-CTIP2 (rat, ab18465, clone# 25B6, Abcam; 1:200), anti-SATB2 (rabbit, ab92446, Abcam; 1:100), anti-HOPX (mouse, sc-398703, clone# E-1, Santa Cruz; 1:200), anti-NG2 (rabbit, AB5320, EMD Millipore; 1:200), anti-CD31 (goat, AF3628, R&D Systems; 1:500), anti-IBA1 (rabbit, 019-19741, Wako; 1:400), anti-IBA1 (goat, ab48004, Abcam; 1:400), anti-SV2 (mouse, SV2-c, clone# not provided by vendor, DSHB; 1:500), anti-PSD95 (rabbit, 51-6900, Invitrogen; 1:250), anti-Myelin Basic protein (MBP) (rabbit, ab218011, Abcam; 1:400), anti-CD44 (rat, MAB6127, clone # IM7.8.1R, R&D Systems; 1:500), anti-EAAT2 (mouse, sc-365634, clone# E-1, Santa Cruz; 1:250), anti-hSPARC-like 1 (HEVIN) (goat, AF2728, R&D Systems; 1:50), anti-PDGFRa (rabbit, ab203491, Abcam; 1:200), anti-hCD38 (mouse, MAB2404, clone# 240742, R&D Systems; 1:200), anti-CXCL10/IP10 (rabbit, MA5-32674, Invitrogen; 1:200), anti-CCL2/MCP-1 (rabbit, NBP1-07035, Novus a biotchnie brand; 1:100), and anti-GLAST (ACSA-1), PE (Miltenyi Biotec, 130-118-483, clone# ACSA-1, 1:50), anti-SOX9 AF647 (ab196184, clone# EPR14335, Abcam; 1:30), anti-Connexin 43 (rabbit, 3512S, Cell Signaling Technology; 1:200)

Secondary antibodies (Jackson ImmunoResearch) used at a dilution of 1:250:

AF488-anti-Chicken, 703-545-155; Cy3-anti-Chicken, 703-165-155; AF647-anti-Chicken, 703-605-155; AF488-anti-Goat, 705-545-147; Cy3-anti-Goat, 705-165-147; AF647-anti-Goat, 705-175-147; AF 488-anti-mouse, 715-545-151; Cy3-anti-mouse, 715-165-151; AF 647-anti-mouse, 715-605-151; AF 488-anti-Rabbit, 711-545-152; Cy3-anti-Rabbit, 711-165-152; AF 647-anti-Rabbit, 711-605-152; AF 488-anti-rat, 712-545-153; Cy3-anti-rat, 712-165-153; AF 647-anti-rat, 712-605-153.

Validation

1. anti-NFIA (rabbit, ab41851, Abcam), 11 studies
2. anti-Ly6C (rat, Clone# ER-MP20, ab15627, Abcam), 31 studies
3. anti-glucose t transporter GLUT1 (rabbit, ab115730, Abcam), 145 studies
4. anti-S100B (rabbit, ab52642, Abcam), 219 studies
5. anti-TBR2/Eomes (rabbit, ab275960, Abcam), 1 study
6. anti-CTIP2 (rat, clone# 25B6, ab18465, Abcam), 567 studies
7. anti-SATB2 (rabbit, ab92446, Abcam), 43 studies
8. anti-IBA1 (goat, ab48004, Abcam), 15 studies
9. anti-Human Nuclear Antigen (HuNu) (mouse, clone#235-1, ab215755, Abcam), 1 study
10. anti-Myel in Basic protein (MBP) (rabbit, ab218011, Abcam), 8 studies
11. anti-SOX2 (rat, clone#Btjce, 14-9811-82, Invitrogen), 35 studies
12. anti-PSD95 (rabbit, 51-6900, Invitrogen), 56 studies
13. anti-GFAP (chicken, AB5541, EMD Millipore), 26 studies
14. anti-NG2 (rabbit, AB5320, EMD Millipore), 197 studies
15. anti-NeuN (rabbit, ABN78, EMD Millipore), 29 studies
16. anti-hHepaCAM (mouse, clone#419305, MAB4108, R&D Systems), 5 studies
17. anti-CD44 (rat, clone # IM7.8.1R, MAB6127, R&D Systems), 5 studies
18. anti-hSPARC-like 1 (HEVIN) (goat, AF2728, R&D Systems), 5 studies
19. anti-CD31 (goat, AF3628, R&D Systems), 180 studies
20. anti-Laminin (rabbit, NB300-144SS, Novus a biotchnie brand), 88 studies
21. anti-Aquaporin 4 (AQP4) (rabbit, AQP-004, Alomone Labs), 80 studies
22. anti-Kir4.1 (rabbit, APC-035, Alomone Labs), 189 studies
23. anti-HOPX (mouse, clone# E-1, sc-398703, Santa Cruz), 64 studies
24. anti-EAAT2 (mouse, clone# E-1, sc-365634, Santa Cruz), 29 studies
25. anti-GFAP (rabbit, 20334, Dako), 69 studies
26. anti-IBA1 (rabbit, 019-19741, Wako), 3329 studies
27. anti-GFP (chicken, GFP-1020, Aves lab), 49 studies
28. anti-hGFAP (mouse, clone# not provided by vendor, Y40420, TaKaRa), 88 studies
29. anti-RFP (Td Tomato) (rabbit, 600-401-379, Rockland), 892 studies
30. anti-SV2 (mouse, clone# not provided by vendor, SV2-c, DSHB), 43 studies
31. anti-PDGFRa (rabbit, ab203491, Abcam), 22 studies
32. anti-hCD38 (mouse, clone# 240742, MAB2404, R&D Systems), 5 studies

- 33. anti-CXCL10/IP10 (rabbit, MA5-32674, Invitrogen), 0 studies
- 34. anti-CCL2/MCP-1 (rabbit, NBPI-07035, Novus biotechnne brand), 14 studies
- 35. anti-GLAST, PE (clone# ACSA-1, 130-118-483, Miltenyi Biotec), 7 studies
- 36. anti-SOX9, AF647 (clone# EPR14335, ab196184, Abcam), 1 study
- 37. anti-Connexin 43 (rabbit, 3512S, Cell Signaling Technology), 271 studies

Eukaryotic cell lines

Policy information about [cell lines and Sex and Gender in Research](#)

Cell line source(s)	Human embryonic stem cells (hESCs) Hues6 (NIH approved ESC line, obtained from HSCI iPS Core), H9 (Wisconsin International Stem Cell (WISC) bank, WiCell research Institute, WA09 cells) and human induced pluripotent cells (hiPSCs) 822 were used in the current study. H9 cells were transduced with pCSC-CAG-GFP lentiviruses and GFP-expressing cells were FACS-sorted as previously described Mansour et al., 2018.
Authentication	All the lines were assessed for genomic integrity by karyotyping (WiCell).
Mycoplasma contamination	All cell cultures were negative for mycoplasma.
Commonly misidentified lines (See ICLAC register)	No commonly misidentified lines were used.

Animals and other research organisms

Policy information about [studies involving animals; ARRIVE guidelines](#) recommended for reporting animal research, and [Sex and Gender in Research](#)

Laboratory animals	NSG male and female mice between 2 and 12 months of age were used in this study. Mice were group-housed 2-5 per cage in autoclaved, individually ventilated cages. The vivarium facility was maintained on a 12-hour light/dark cycle with lights on at 0600. Temperature was maintained at approximately 21C. Humidity in the facility was monitored but not controlled.
Wild animals	No wild animals were used in this study.
Reporting on sex	Both male and female mice were used for experiments. Male and female animals were randomly assigned to experiments.
Field-collected samples	No field samples were collected in this study.
Ethics oversight	All animal experiments described in the current study were approved by the Institutional Animal Care and Use Committee (IACUC) at the Salk Institute for Biological Studies (12-00022) and were conducted in compliance with the National Institute of Health's Guide for the Care and Use of Laboratory Animals.

Note that full information on the approval of the study protocol must also be provided in the manuscript.